Université catholique de Louvain

École polytechnique de Louvain (EPL)

Calibration of the SKA-low antenna array using drones

Dissertation presented by
Loïc Van Hoorebeeck

for obtaining the Master's degree in
Mathematical Engineering

Supervisor(s)
Christophe Craeye, François Glineur

Reader(s)
Ha Bui Van, Eloy de Lera Acedo , Claude Oestges

Academic year 2017-2018

“Attitude is a little thing that makes a big difference.”

Winston Churchill

Université Catholique de Louvain

Abstract

Ecole Polytechnique de Louvain

Calibration of the SKA-low antenna array using drones

by Loïc Van Hoorebeeck

Due to the always higher demand for precision and survey speed coming from the astronomers, it is required to lean on always bigger radio telescopes. The latter need accurate calibration to ensure the capture of high quality images. In particular, the Square Kilometre Array (SKA), the world's largest radio telescope currently in development with expected deployment by late 2020s [1], will need precise and accurate calibration. Natural calibration, e.g. Self-Cal algorithm, is widely used in the radio astronomy literature and allows the calibration of several SKA pathfinders, e.g. the Very Large Array (VLA) and Murchison Widefield Array (MWA). The increased sensitivity and the very large number of antennas of the SKA reduce the hope of a sole self-calibration. Research with artificial sources carried by a Unmanned Aerial Vehicle (UAV) has already led to successful far-field calibrations of radio telescopes [2, 3]. In this work, we show a near-field calibration procedure applied on a SKA station composed by 256 log-periodic antennas. A comparison is also made with a far-field calibration procedure. Two antennas mounted on a UAV act as calibration sources. Several flight strategies are studied with uncertainties on the position and UAV attitude. A maximum error between exact and modeled pattern of 40 dB with respect to the main lobe is obtained for a Gaussian noise of standard deviation of 5 cm. We show that near-field calibration enables to correctly model embedded element and array pattern. In comparison with a far-field proceeding, the flight distance is substantially reduced and the collected data carry more information. Near-field calibration offers a new window which has not been yet fully explored and is expected to give promising results.

Acknowledgements

First, I would like to thank my advisors, Christophe Craeye and François Glineur, for the precious guidance throughout this work.

I also would like to thank Ha Bui Van for his patience and explanations, and Jean Cavillot for his assistance.

Then, I express all my gratitude to Marie Valenduc for the help and the careful rereading as well as Geoffroy van der Rest for the passionated debates about drones and composite materials.

Finally, I acknowledge my parents for their unfailing support.

Contents

List of Figures

List of Tables

Abbreviations

AUT	**A**ntenna **U**nder **T**est
AAVS0	**A**perture **A**rray **V**erification **S**ystem **0**
CS	**C**oordinate **S**ystem
FF	**F**ar **F**ield
FOV	**F**ield **O**f **V**iew
GCV	**G**eneralized **C**ross - **V**alidation
GNSS	**G**lobal **N**avigation **S**atellite **S**ystem
HARP	**HAR**monic **P**olymonial
IMU	**I**nertial **M**easurement **U**nit
IXR	**I**ntrinsic Cross-Polarization (**X**) **R**atio
LSQI	**L**east **S**quares minimization with a **Q**uadratic **I**nequality constraint
LFAA	**L**ow - **F**requency **A**perture **A**rray
LNA	**L**ow - **N**oise **A**mplifier
MBF	**M**acro **B**asis **F**unction
MAD	**M**edicina **A**rray **D**emonstrator
MWA	**M**urchison **W**idefield **A**rray
NF	**N**ear **F**ield
QO	**Q**uasi **O**ptimality criterion
SKA	**S**quare **K**ilometer **A**rray
SKALA	**S**quare **K**ilometer **A**rray **L**og-periodic **A**ntenna
TSVD	**T**runcated **S**ingular **V**alue **D**ecomposition
UAV	**U**nmanned **A**erial **V**ehicle
VLA	**V**ery **L**arge **A**rray

Symbols

$\mathbf{c}^i$	calibration coefficient	
$cf^i_{i_m,i_a}$	MBF coefficients computed by HARP	
D	array diameter	[m]
$\mathbf{F}^i_v$	embedded element pattern	
f_{obj}	objective function	
h	horizontal polarization	
i	ON antenna while the other are terminated	
i_a	current antenna	
i_e	current experiment	
i_m	current MBF	
k	wave number	
N_a	number of antennas	
N_m	number of MBF	
N_e	number of experiments	
$\mathbf{p}_{v,i_m}$	radiation pattern of the MBF	
(u_x, u_y, u_z)	unit vector in the direction θ, φ of interest	
v	vertical polarization	
(x_{i_a}, y_{i_a})	position on the antenna	[m]
θ	zenith angle	[rad]
σ_m	standard deviation of the error on the position	[m]
σ_a	standard deviation of the error on the attitude	[rad]
φ	azimuth angle	[rad]

Chapter 1

Introduction

Man has always been captivated by the sky, from Mesopotamia to Mongolian steppes and through all eras, humans have consistently gazed above. Today makes no exception: little children dream to be astronauts, the space race is rerunning with — this time — planet Mars as target, and a huge radio telescope is under construction, challenging scientists and engineers across the whole planet. This thesis aims at contributing to this colossal project.

The SKA radio telescope. Most people are familiar with the concept of a telescope: one looks through lenses and is suddenly able to distinguish very small details. A radio telescope works analogously, except that it captures electromagnetic radiations outside the visible spectrum. In this way, the resulting images can be very different from traditional telescopes and in addition, it is possible to obtain images during the day or when the sky is cloudy.

In this work, we consider a specific radio telescope: the Square Kilometre Array (SKA). The SKA is an antenna array to be built in Australia and South Africa. Despite its name, the total collection area of the SKA will be well over one square kilometre after completion. The SKA will use thousands of "dishes" and up to a million of low-frequency and mid-frequency antennas.

Rather than just bundled in a central core region, the telescopes will be arranged in multiple spiral arm configurations, with the dishes extending to large distances from the center. This will create a long baseline interferometer array similar to the very large array (VLA) located in New Mexico.

Splitting the antennas this way, the interferometry approaches enable astronomers to imitate a telescope with a resolution comparable to that of a virtual instrument whose size is equal to the maximum separation between the telescopes in the array. Therefore, instead of building a huge dish, the capabilities of an antenna array are preferred, in the sense that it enables the system to act either as one gigantic telescope, or as multiple smaller telescopes, allowing high flexibility [1].

The SKA can be split in three parts: two aperture antennas arrays, the SKA-low and the SKA-mid, and finally the dishes. In this thesis, we focus on the calibration of the SKA-low stations (Figure 1.1), which cover the frequencies in the range $[50 - 350]$ MHz. This Low-Frequency Aperture Array (LFAA) has no moving parts and is therefore a true all-electronic telescope. One pathfinder is the Low-Frequency Array or LOFAR telescope completed in 2012 by ASTRON. The LOFAR consists of 45 stations, the core of which is located in the Netherlands, with stations also in Germany, France, the UK and Sweden, thus creating long baselines (the separation between any two stations as seen from the radio source is called a baseline).

The SKA project aims at various goals, this radio telescope will be used to answer fundamental questions of science such as: how did the Universe form and expand ? Are we alone in the universe ? What is the nature of "dark matter" and "dark energy" ? The SKA will also be used to challenge Einstein's theory of general relativity [1].

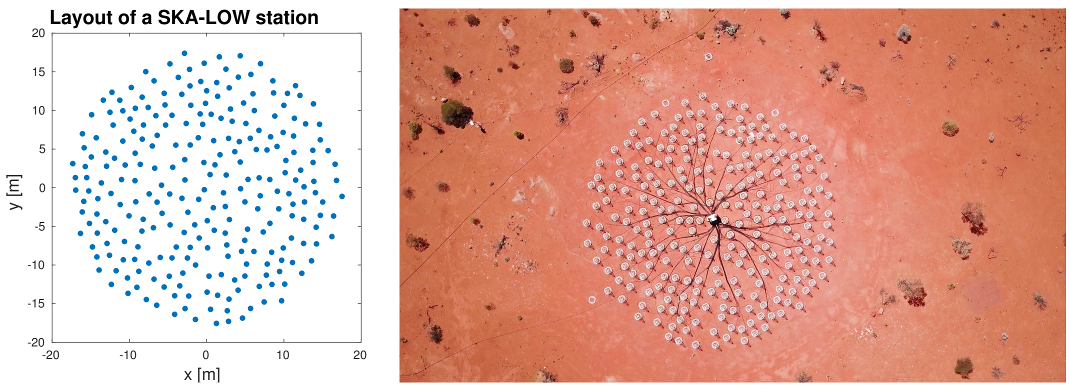

Figure 1.1: Layout of a SKA-low station. Each station consists of 256 antennas irregularly arranged. The left figure represents the station layout used in this work and the right figure is an actual picture of the first SKA-low prototype station completed on site [4].

Interferometer description. A radio interferometer is an array of "elements". The elements can be antennas, or antennas arrays in the case of the SKA-low. This device emulates a discretely-sampled telescope of large aperture or, put differently, a radio interferometer can be seen as a single telescope with a very large and not entirely filled aperture. The maximum aperture size is equivalent to the maximum distance, or baseline, between any pair of its component elements. This large "synthesized" aperture is only tested at the locations at which an element exists. This benefits from the rotation of the Earth moving the elements, therefore multiplying the sampling. This is known as "Earth rotation aperture synthesis". The size of the synthesized aperture governs the resolution, or "beam size", of the radio telescope. The larger the aperture, the smaller the resolution [5].

Calibration definition. In general, calibration consists in comparing measurements from a device under test with known measurements. As an illustration, let us suppose we want to calibrate a scale: this can be done by weighing a one kilogram standard and comparing the obtained result with the true weight. In this study, however, the term calibration refers simultaneously to the comparison between expected and obtained measurements, and to the adjustments made to the device in order to correct the observed error.

Calibration goal. In this context, the goal of the calibration procedure is to find the response of the telescope to the sky, and to remove as much and as accurately as possible, the known and undesired bright sources, e.g. the sun, from the visibilities. The visibilities are the discrete components of the spatial frequency spectrum of the observed source brightness distribution. A visibility is defined for each baseline and thus for each pair of stations. Imaging of the residual data then yields a minimally contaminated view of the unknown flux density, in which the relevant information lies. Given the high sensitivities that are targeted, severe demands are placed upon the accuracy with which the station patterns are known [6]. The calibration procedure is more detailed in the next section.

A legit question to ask is: *what* is going to be calibrated? As explained before, the SKA-low will consist of several hundreds of stations, each composed of 256 antennas. In this framework, an element can be an antenna or a whole station, and multiple calibration levels appear. This work is devoted to the calibration of a single station, but the outcomes will be used in the whole array calibration.

Calibration is crucial in a project such as the SKA. The purpose of building this gigantic telescope is to reach a *hitherto* unattainable sensitivity. The calibration should hence be made at a similar level. Figure 1.2 illustrates the need of calibration.

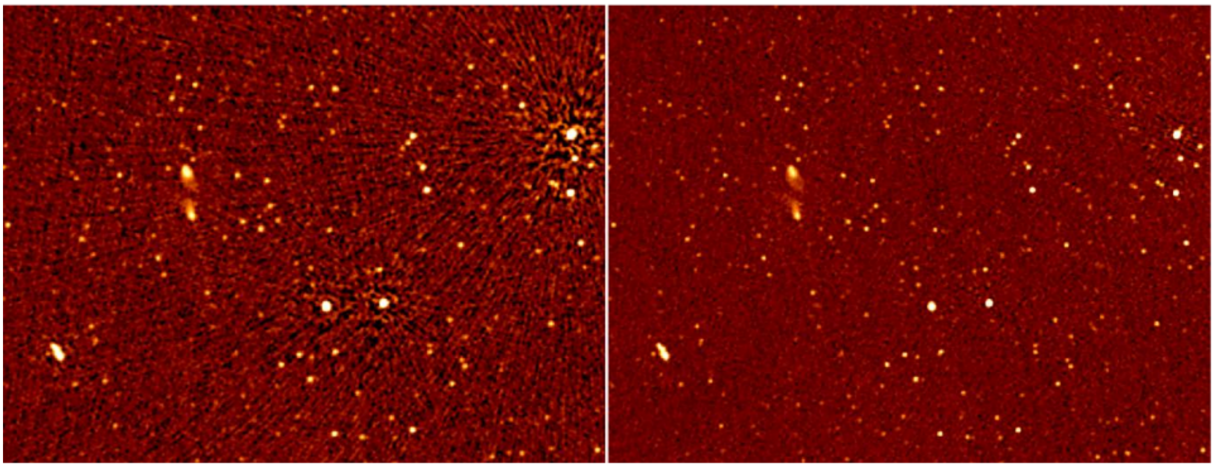

FIGURE 1.2: Uncalibrated (left) and calibrated images (right) of the Murchison Widefield Array (MWA) [7]. The MWA is a low frequency (80 — 300 MHz) radio telescope operating in Western Australia and one of the SKA-low precursor.

This work focuses on calibration with artificial sources. It differs from calibration with natural sources (self calibration) by the use of a Unmanned Aerial Vehicle (UAV) carrying sources. In order to evaluate the calibration quality that can be expected, two physical quantities are inspected: the embedded element pattern (EEP) and the array pattern modulus (AP). The array pattern modulus can be defined as the absolute value of the electric field far away from the array and is often normalized:

$$AP(\theta, \varphi) = \frac{\lim_{r\to\infty} |\mathbf{E}(r,\theta,\varphi)|}{\max_{\theta,\varphi} \lim_{r\to\infty} |\mathbf{E}(r,\theta,\varphi)|} \, . \tag{1.1}$$

The EEP is defined similarly but rather than turning on every antennas, a single antenna is ON and the other are passively terminated. Remark that the AP can be computed as the weighted sum of every EEP. If coupling effects are negligible, the EEP is similar to the isolated antenna pattern: such an approximation is not valid for the SKA-low. We define the error

$$e_{\theta,\varphi} = 10\log_{10}\left(\left|\mathbf{E}_v - \bar{\mathbf{E}}_v\right|^2 + \left|\mathbf{E}_h - \bar{\mathbf{E}}_h\right|^2\right) - 10\log_{10}\max_{\theta,\varphi}\lim_{r\to\infty}|\mathbf{E}(r,\theta,\varphi)| \, , \tag{1.2}$$

with $\mathbf{E}_v$, $\mathbf{E}_h$ respectively the vertical and horizontal polarization of the exact field and $\bar{\mathbf{E}}$ the calibrated field. In order to evaluate whether we are close to the reference pattern, we outline two figures of merit

$$e_M = \max_{\theta,\varphi}\{e_{\theta,\varphi}\} \, , \tag{1.3}$$

$$\mu_e = \mathbb{E}\{e_{\theta,\varphi}\} \, . \tag{1.4}$$

The knowledge of the maximum error (e_M) is important given that it allows a worst-case analysis. However, this maximum is computed over a finite number of points and it is possible to miss it. In this way, the mean error (μ_e) is equally important. A comparison of both figures indicates whether the calibration is uniform or not: $e_M \approx \mu_e$ implies that every direction is similarly estimated and $e_M \gg \mu_e$ indicates that some directions are better calibrated.

In this thesis, we try to assess first if an artificial calibration is recommended for the SKA-low. Then, we evaluate the impact of the UAV path and finally judge if a calibration far or close to the array should be explored. In some sense, it can be viewed as technical specification on the uncertainty on position and attitude, which a UAV should satisfy in a real calibration campaign. The study made here on the UAV path can also provide practical information about the UAV flight time and UAV battery size.

Calibration procedure. The calibration procedure is the following: a UAV mounted with two antennas hovers above the SKA-low station and collects measurements of the fields at positions (x, y, z). These measurements contain noise mainly due to the uncertainties linked to the UAV position and attitude. The noisy positions are written as $(\tilde{x}, \tilde{y}, \tilde{z})$. A set of coefficients is computed by comparing the measurements $E(x, y, z)$ with the computed fields $\tilde{E}(\tilde{x}, \tilde{y}, \tilde{z})$ at these noisy positions. The computation of the fields is performed using the software HARP described in Section 2.4. The coefficients are calculated in the least-squares sense. This procedure is summarized in Figure 1.3.

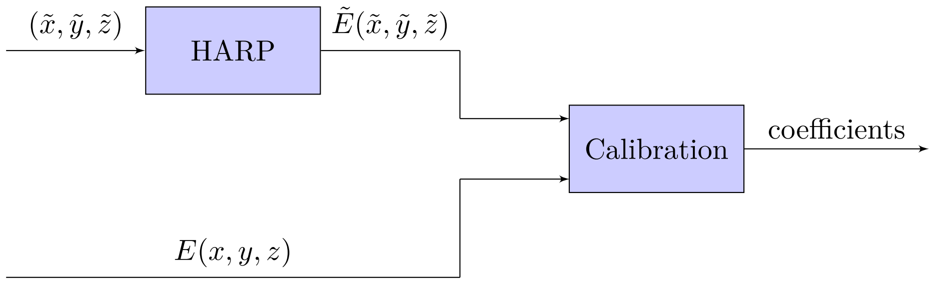

FIGURE 1.3: Scheme of calibration procedure.

The error is then evaluated between the exact and model pattern. The discussion essentially concerns the two figures of merit: the maximum and the mean error.

It is assumed here that the fields computed with the software HARP are exact and that errors other than the ones due to position and attitude noises are neglected. This means that we consider $\tilde{E}(\tilde{x}, \tilde{y}, \tilde{z}) = E(\tilde{x}, \tilde{y}, \tilde{z})$.

Outline of the thesis. This work is organized as follows: first, we present the state-of-the-art calibration techniques. Self-calibration has had a strong influence but artificial calibration is gaining weight for a couple of years and has already provided some successful results. We outline the major challenges of calibration and the tool used in this work for the simulation: the HARP software. Chapter 3 is a first calibration attempt: it aims at operating the UAV in the far-field region. Only noise on the position is evaluated: the UAV is assumed to fly in a horizontal plane with antennas aligned with the array antennas. The next chapter, devoted to near-field calibration, explains how to model a calibration much closer to the array. Then, Chapter 5 extends the model by taking into account the UAV attitude. The impact of the noise on the position and on the attitude is evaluated. Finally, Chapter 6 shows how some mathematical tools can highly improve the calibration in the case of an ill-posed problem.

Chapter 2

State of the art

In this section the state-of-the-art techniques used for the calibration of an antenna array are investigated.

This chapter is organized as follows: firstly we introduce the major causes of non-ideality leading to the need for calibration. Then the different levels of calibration with direct application to the SKA-low are outlined, followed by the two different possible calibrations: from natural or artificial sources. We also present the works that already have been carried out in the latter case, and more specifically the differences between *far-field* and *near-field* calibrations. Finally, the software used for the pattern simulations, HARP, is described.

2.1 Non-idealities of an antenna array

We study here what typical behaviour can be expected from the SKA and where those non-idealities lie in the SKA block-chain [8]. Some of these effects are time-dependent and hence *a priori* calibration cannot expect to work.

Receiver complex gain. Radioastronomy signals are very weak and the used devices need therefore to be very sensitive. This requires low-noise amplifiers (LNA), since the noise is inversely proportional to the thermal noise temperature [8]. Coupled with the transmission of the received signal to the processing core as well as the environmental conditions (e.g. temperature, environmental effects, mutual coupling, effect of soil) this induces a complex gain, phase and amplitude of the receiver [2].

Instrumental response. The radiation pattern of the individual element, which may be an antenna or more globally an entire station, cannot be known exactly. This is expressed as uncertainties on the beam pattern. Indeed, even when the beam is focused on the desired source, the beam pattern shows sensitivity in other directions due to the sidelobes. This may degrade the signal if a much more powerful source, for instance the sun, is located in the direction of a sidelobe. The algorithms responsible for the beam forming can avoid sensitivity in these specific directions; this is called nulling. However, it relies on the accurate knowledge of the patterns. This may not be the case if the array is not properly calibrated.

Propagation effects. The signal coming from the sky passes through the atmosphere. However, it is well known that the troposphere and ionosphere induce time-varying refractions and diffractions. Those phenomena are due to turbulence as well as the presence of plasma and yield distortions similar to the ones we observe while looking at the ceiling lights from the bottom of a swimming pool [8].

Contingencies. Occasional failures of the components change the layout of active antennas [6].

2.1.1 Ionospheric effects

One of the major calibration challenges at the frequencies of interest are the ionospheric effects. The latter appear at different levels: at the station level and at the whole radio telescope level. Here we follow Lonsdale's convention [6] by defining three characheristic lengths: A, the instrument aperture; S, the size of ionospheric irregularities of sufficient magnitude to degrade an uncalibrated image to an unacceptable level and finally V the station field of view (FOV) at ionospheric heights. Four different categories can be studied, depending on how these scale lengths are ordered.

Regime 1: $A \ll S$, $V \ll S$. [Figure 2.1 - Top Left] All stations and all FOV sample the same part of the sky: the ionospheric effects do not deteriorate the uncalibrated image. This is not the case in large arrays such as the SKA-low: in this regime, the array operates more as a single dish than as an interferometer. The FOV is small as well as the baselines [9].

Regime 2: $A \gg S$, $V \ll S$. [Figure 2.1 - Top Right] Each station observes through a different ionospheric layer but at station level, the lines of sight sample the same ionospheric delay. In this regime, the so-called Self-Cal procedure, described in Section 2.2, can work satisfactorily [6]. The FOV is small and the baselines are large.

Regime 3: $A \ll S$, $V \gg S$. [Figure 2.1 - Bottom Left] The stations are bundled and therefore see the same ionospheric layer. However, the FOV is larger than the ionospheric irregularities. This regime occurs when the interferometer configuration is very closely packed into a *core*. The

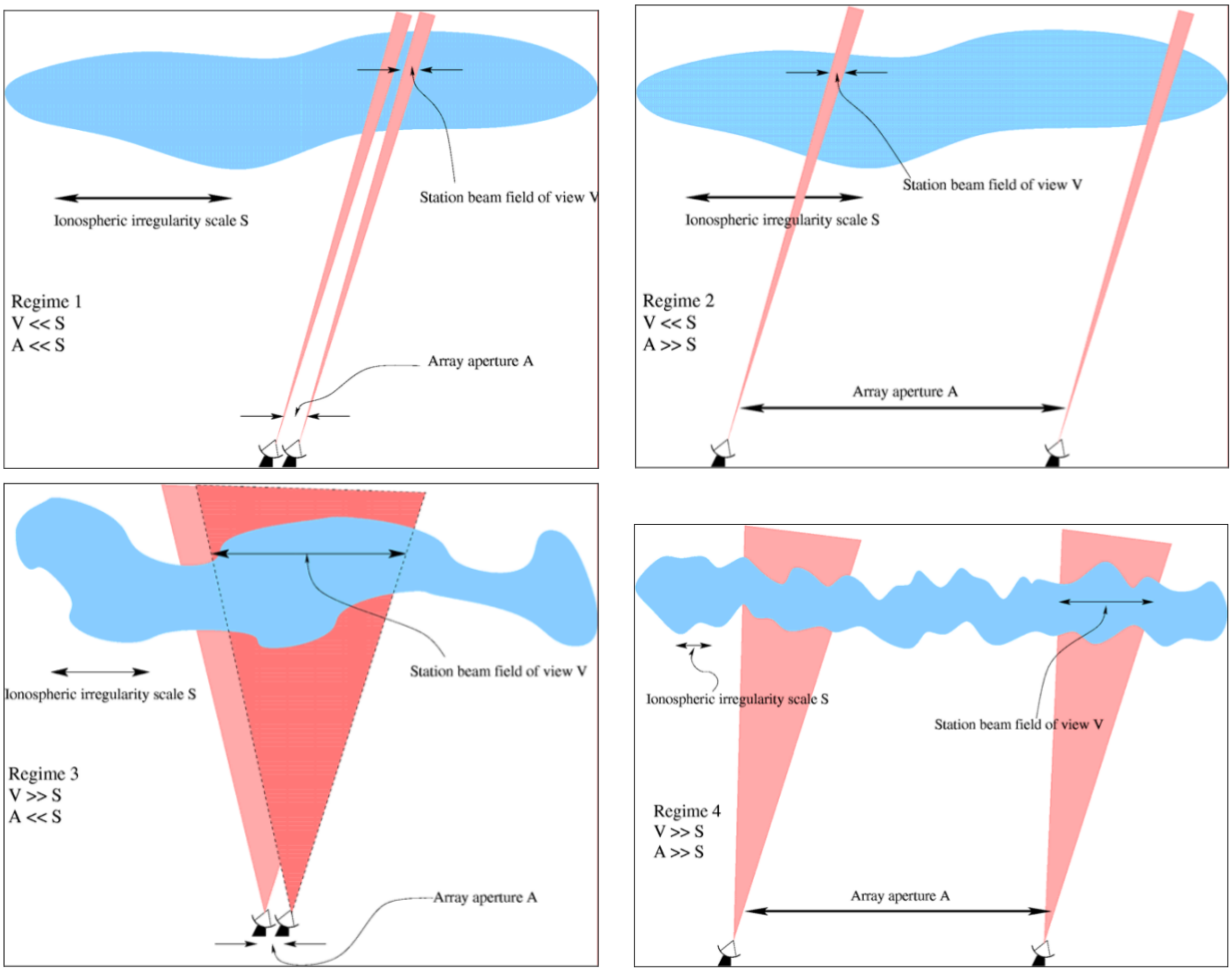

FIGURE 2.1: The four differents regime as considered by Lonsdale [6]. From left to right and top to bottom: Regime 1, 2, 3 and 4.

SKA-low is going to be built in such a way: 75% of the stations are located in a disk of radius 4 km with the remaining stations located on three spiral arms extending out to 50 km [1]. The FOV is large and the baselines are short.

Regime 4: $A \gg S$, $V \gg S$. [Figure 2.1 - Bottom Right] All stations see different parts of the ionosphere and every source is seen through different ionospheris domains. This is the most general case and occurs in very large arrays such as the LOFAR (Low-Frequency Array) or the SKA-low. The core belongs to regime 3 while the remaining stations belong to regime 4. The FOV is large, as well as the baselines.

2.2 Self-calibration

This conventional algorithm is a technique allowing one to compute efficiently the complex gain of each antenna in an array. It is a closed-loop algorithm working by analyzing the difference between predicted response and measured data from a known source. Note that this efficiency can only be achieved when the gain does not vary accross the FOV, i.e. in regimes 1 and 2 [6]. Nonetheless, a multisource self-calibration procedure has been presented in [9] in the case of regime 3.

The self-calibration method is based on the measurement equation [10]

$$V_{i,j}(t) = g_i(t)\, g_j^{\mathrm{H}}(t)\, V^{\mathrm{true}}(t) + \epsilon_{i,j}(t)\,, \tag{2.1}$$

with $V_{i,j}$ the visibility measured between antenna i and j, g_i the complex gain of antenna i, $\epsilon_{i,j}$ the additive noise and V^{true} the true visibility. H stands for the conjugate transpose. Applied in a closed-loop way, Algorithm 1 is obtained.

Algorithm 1 Self-Cal algorithm according to [10]

1: Create an initial source model, typically from an initial image
2: Find antenna gains by least squares
3: Apply gains to correct the observed data
4: Create new model visibilities V^{mod} from the corrected data
5: Go to (2), unless current model is satisfactory

2.3 Measurement campaign

To this day, several calibration methods have been evaluated to calibrate large antenna arrays: self-calibration [9], far-field with UAV [2] and near-field [11]. More specifically, a micro-UAV platform has been used to characterize Intrinsic Cross-Polarization Ratio (IXR) in [12] to obtain Antenna Pattern of Biconical and Log-Periodic Antennas in [13] and to perform calibration and pattern characterization [3] for the Medicina Array Demonstrator (MAD) and in [2] for the AAVS0 (Aperture Array Verification System 0). These measurement campaigns have been realized in the far field and have shown very satisfying results. However, the MAD is a 3×3 regular array and the AAVS0 is a 16-antennas non-regular array. This limited number of antennas allows the UAV to fly at a relatively low altitude, while satisfying the far-field condition. However, every SKA-low station will have 256 antennas placed in a random configuration into a disk of 35 m diameter. This induces a much larger altitude in order to fulfill the far-field condition. Finally, a near-field single antenna calibration is presented in [14].

2.4 HARP software

In this work, real measurements are not available. Therefore, a tool is needed to simulate the embedded element pattern (EEP) and array pattern (AP). We use here the Macro Basis Functions (MBF) framework as explained in [11, 15] via the software HARP (HARmonic Polynomial).

This tool, presented in [16], "relies on the MBF and an interpolatory technique to compute the interactions between MBFs" [16] and therefore evaluates the entries of the Method of Moments (MoM) matrix. It has been tested on a non-regular array with SKALA antennas and shows results similar to those obtained with commercial software (CST Microwave Studio [17] and WIPL-D [18]) with several orders of magnitude improvement in computational time: from 96 hours with CST or WIPL-D to 30 seconds with HARP [16]. The SKALA model used in HARP (Figure 2.3) consists in a wire mesh comprising 1218 basis functions. In order to save computational time, the MBF technique allows a significant dimension reduction. This number should increase with the frequency. In this work, a single frequency of 140 MHz has been studied with $N_m = 40$ MBFs.

Method of Moments (MoM). Maxwell's equations often lead to integral equations with complex geometry, which implies that no analytical solution is available. The MoM is a numerical technique allowing the conversion of these integral equations into a linear system of equations [19]. In order to illustrate this method, the MoM is applied on a general problem. Assuming an unknown physical quantity q, for instance the electric potential or the electric field, that can be computed using an integral equation on geometry G and a known physical quantity ψ,

$$\psi = \mathcal{L}[q\,,\,G]\,, \tag{2.2}$$

with $\mathcal{L}$ a linear operator in q, for instance $\mathcal{L}[q, G] := \int_0^L q(x)\,dx$. Assume the geometry is a simple wire (Figure 2.2a). As mentioned above, we may not be able to solve analytically Equation (2.2) on the geometry G. The MoM is then applied. Firstly, this wire is segmented into N sections with middle points x_n, $n = 1 \ldots N$ (Figure 2.2b). Then, a set of basis functions $B := \{f_n(x) : n = 1 \ldots N\}$ is chosen. Figure 2.2c depicts a choice of triangular basis functions but other choices are possible, e.g. pulses. We project q on the finite dimensional space spanned by the basis B,

$$q \approx \sum_{n=1}^{N} a_n f_n\,, \tag{2.3}$$

with weights $\{a_n := q(x_n) \quad | \quad n = 1 \ldots N\}$. By linearity of $\mathcal{L}$, Equation (2.2) becomes

$$\psi \approx \sum_{n=1}^{N} a_n\,\mathcal{L}[f_n\,,\,G]\,, \tag{2.4}$$

with residual

$$R := \psi - \sum_{n=1}^{N} a_n\,\mathcal{L}[f_n\,,\,G]\,. \tag{2.5}$$

We define an inner product or *moment*

$$\langle f_1, f_2 \rangle = \int_G f_1\,f_2\,, \tag{2.6}$$

where f_1 and f_2 are integrable on G. Finally, testing with M *test functions* f_m and requiring the inner product with the residual function to be zero yields[1]

$$\sum_{n=1}^{N} a_n \langle \mathcal{L}[f_n, G]\, ,\, f_m \rangle = \langle \psi, f_m \rangle \qquad \forall\, m = 1 \dots M. \tag{2.7}$$

This leads to a linear system of equations

$$\mathbf{Za} = \mathbf{b}\,, \tag{2.8}$$

with the $\mathbf{Z}$ matrix, called *impedance* or MoM matrix, defined by

$$z_{mn} = \langle \mathcal{L}[f_n, G]\, ,\, f_m \rangle\,, \tag{2.9}$$

and the right hand-side $\mathbf{b}$ given by

$$b_m = \langle q, f_m \rangle\,. \tag{2.10}$$

Finally, the integrals are evaluated using quadratures.

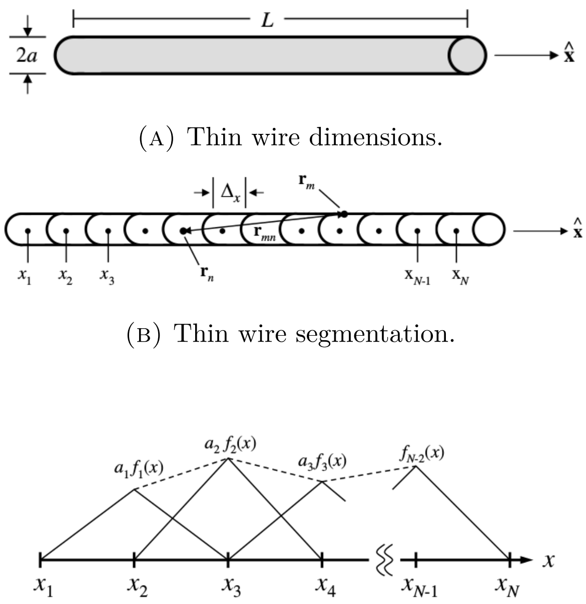

(A) Thin wire dimensions.

(B) Thin wire segmentation.

(C) Triangle functions.

FIGURE 2.2: Illustration of MoM basis functions decomposition. Figures from [19].

Macro Basis Functions (MBF). The MoM is applied to the SKALA antenna with 1218 basis functions. Using Gaussian elimination to solve N_a times, one for each antenna, the Equation (2.8) yields a complexity of $\mathcal{O}(N_a N_b^3)$ where N_a is the number of antennas and N_b the

[1] This procedure is very similar to the Galerkin method. The key property is the orthogonality with the residual, i.e. *Galerkin orthogonality*.

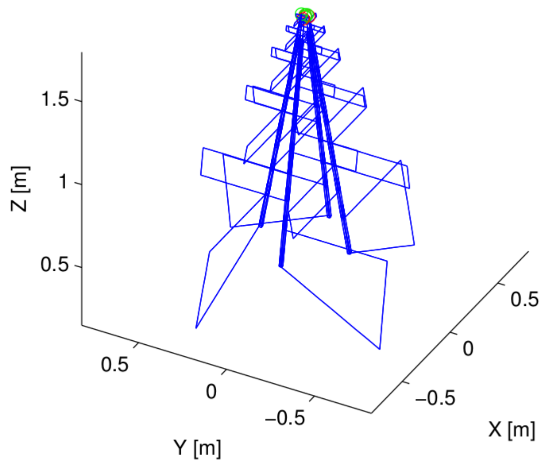

FIGURE 2.3: Wire mesh of the SKALA. This antenna consists of 4 arms supported by 4 spines. The feeds are located on top, providing two polarizations [16].

number of elementary basis functions. The MBF approach enables to reduce this computational time by replacing the original set of elementary basis functions by a new set of functions, the macro basis functions, obtained through the solution of smaller problems [16]. The resulting compressed problem has now a complexity of $\mathcal{O}(N_a N_m^3)$ with N_m the number of MBFs. Given that $N_m \ll N_b$, this highly accelerates the method.

Pattern calculation. Using the MBF framework, the vertical polarization of the EEP of antenna i can be expressed as follows [16],

$$F_v^i(\theta, \varphi) = \sum_{i_m=1}^{N_m} \sum_{i_a=1}^{N_a} cf^i_{i_m, i_a}\, p_{v,i_m}(\theta, \varphi)\, e^{jk(x_{i_a} u_x + y_{i_a} u_y)}\,, \tag{2.11}$$

where (x_{i_a}, y_{i_a}) is the position of the antenna i_a, (u_x, u_y, u_z) is a unit vector in the direction (θ, φ) of interest, p_{v,i_m} is the vertical polarization of the pattern of MBF i_m and $cf^i_{i_m,i_a}$ the coefficient for MBF i_m on antenna i_a when only antenna i is ON. Please notice that every MBF is expressed through the 1218 elementary basis functions.

Finally, the whole array pattern is computed as the weighed sum of the EEP. For instance the vertical polarization is given by

$$F_v(\theta, \varphi) = \sum_{i=1}^{N_a} w_i\, F_v^i(\theta, \varphi)\,, \tag{2.12}$$

with w_i the weight of antenna i. The weights depend on the direction of scan.

Chapter 3

Far-field calibration

This chapter is devoted to the analysis of measurements far away from the antenna array. We assume that at every measurement, the UAV height satisfies the far-field condition i.e.

$$r \gg \frac{2D^2}{\lambda}$$

the right hand-side being the FRAUNHOFER distance where D is the diameter of the array and λ the wavelength. In the case of a SKA-low station, the diameter is about 35 m and the wavelength goes from 0.85 m (350 MHz) to 6 m (50 MHz) [1]. The worst-case scenario requires flying above 3 km.

In this chapter, we assume a UAV device able to fly at this altitude. At first we do not worry about some obvious restrictions such as the battery lifetime of the device. Moreover, we assume a horizontal flight and recording of two components of the electric field via two antennas placed on the UAV. A noise on the device position is considered during the measurements. Notice that we are interested in *a posteriori* position. Indeed, the trajectory tracking by the UAV can be seen as a dynamical system. We do not expect the UAV to perfectly follow the input trajectory. This is not a serious issue as long as the true position is recorded. This *a posteriori* position is the input of our calibration system. The noise then corresponds to the uncertainty on the measured position of the UAV.

This chapter is organized as follows: first of all, we explain how to use some far-field measurements to find the calibration coefficients. Then, we inspect the case of a single coefficient per antenna and the case of multiple coefficients. Finally, we present flight strategies used in this work and show some calibration outcomes.

3.1 Methods

3.1.1 Calibration with exact measurements on perturbed positions

Let us first explain what the term *measurement* refers to in this context. The whole array pattern is the superposition of every EEP. Due to coupling between antennas, every single antenna has a contribution to every EEP. As mentioned before, we consider a UAV flying high enough to satisfy the far-field condition. Throughout this report, we will extensively use the Reciprocity theorem whose full explanation can be found in [20]. Following [20], "First, it establishes a simple relation between the properties of transmitting and receiving antennas, which permits a deduction of receiving-antennas properties from those of the transmitting antennas, and vice versa. Second, it establishes an interchangeability in the performance of receiving and transmitting antennas.".

In this work, the reciprocity theorem is used in this way: instead of considering the UAV to send a pulse, which is received by the antennas, we consider that each antenna sends a pulse, which is received by both antennas of the UAV. Moreover, by virtue of Maxwell's equations linearity, we can study independently each of these pulses. Inspecting this setup, we observe that N_a measurements are collected for every pulse sent by the UAV. This is well appreciated because we consider a calibration coefficient $c^i_{i_a}$ for the contribution of each antenna i_a to every EEP of antenna i. Hence, the terminology *experiment* is used for the pulse transmission associated with a single UAV position, leading to N_a *measurements*. We will keep this convention throughout this thesis. Finally, we notice that, with at least N_a independent experiments, we can find the N_a^2 calibration coefficients $\mathbf{c}$ through the N_a^2 measurements.

3.1.1.1 One coefficient for each antenna

Keeping in mind the configuration stated above, let i denote the antenna "ON" with i fixed. Please note that in this study, the electric field is expressed in terms of horizontal and vertical polarization, this is known as Ludwig II definition [21]). For the sake of clarity, both components are described separately and then the sum of the squares is computed. The first component of antenna i EEP is

$$\mathbf{F}^i_v = \sum_{i_m=1}^{N_m} \sum_{i_a=1}^{N_a} cf^i_{i_m,i_a} \, \mathbf{p}_{v,i_m} \, e^{jk(x_{i_a}u_x + y_{i_a}u_y)} \,, \tag{3.1}$$

with phase reference in the center of the array and quantities as defined in Equation (2.11). Here, vectorial notation is used given that the field is expressed for every experiment point. The horizontal component is similar,

$$\mathbf{F}^i_h = \sum_{i_m=1}^{N_m} \sum_{i_a=1}^{N_a} cf^i_{i_m,i_a} \, \mathbf{p}_{h,i_m} \, e^{jk(x_{i_a}u_x + y_{i_a}u_y)} \,. \tag{3.2}$$

Let us now consider the calibrated pattern. Assume complex coefficients acting on the amplitudes and phases of the pattern. The vertical polarization of the calibrated EEP, written $\overline{\mathbf{F}_v^i}$, becomes

$$\overline{\mathbf{F}_v^i} = \sum_{i_m=1}^{N_m} \sum_{i_a=1}^{N_a} cf_{i_m,i_a}^i \, \mathbf{p}_{v,i_m} \, e^{jk(x_{i_a}u_x + y_{i_a}u_y)} c_{i_a}^i \tag{3.3}$$

$$= \sum_{i_a}^{N_a} \mathbf{b}_{v,i_a}^i \, c_{i_a}^i = \mathbf{B}_v^i \, \mathbf{c}^i \, . \tag{3.4}$$

Notice that $\mathbf{B}_v^i$ columns are defined by $\mathbf{b}_{v,i_a}^i := \sum_{i_m=1}^{N_m} cf_{i_m,i_a}^i \mathbf{p}_{v,i_m} e^{jk(x_{i_a}u_x + y_{i_a}u_y)}$ and hence, $\mathbf{B}_v^i$ is a matrix in $\mathbb{C}^{N_e \times N_a}$ where N_e is the number of experiments. The columns of $\mathbf{B}^i$ can be seen as **B**asis patterns of a finite dimensional vectorial set. Henceforth, $\mathbf{c}^i$ contains the coordinates of $\overline{\mathbf{F}_v^i}$ in this basis. For each ON-antenna i we solve a different optimization problem,

$$\min_{\mathbf{c}^i \in \mathbb{C}^{N_a}} ||\mathbf{F}_v^i - \overline{\mathbf{F}_v^i}||_x + ||\mathbf{F}_h^i - \overline{\mathbf{F}_h^i}||_x \, . \tag{3.5}$$

Using the Euclidean norm, i.e. $||\cdot||_x = ||\cdot||_2$, it comes

$$\min_{\mathbf{c}^i \in \mathbb{C}^{N_a}} \left(\sum_{i_e=1}^{N_e} \left(\left| F_{v,i_e}^i - \sum_{i_a=1}^{N_a} B_{v,i_e,i_a}^i \, c_{i_a}^i \right|^2 \right) \right)^{1/2} + \left(\sum_{i_e=1}^{N_e} \left(\left| F_{h,i_e}^i - \sum_{i_a=1}^{N_a} B_{h,i_e,i_a}^i \, c_{i_a}^i \right|^2 \right) \right)^{1/2} . \tag{3.6}$$

Some remarks about expression (3.6) can be made. First, it is an unconstrained optimization problem. The objective function is convex but not differentiable with respect to variable $\mathbf{c}$. In order to obtain a simpler optimization problem, we slightly change the objective function by taking the sum of the squares, i.e.

$$f_{\text{obj}}(\mathbf{c}^i) = \left|\left|\mathbf{F}_v^i - \overline{\mathbf{F}_v^i}\right|\right|_2^2 + \left|\left|\mathbf{F}_h^i - \overline{\mathbf{F}_h^i}\right|\right|_2^2 . \tag{3.7}$$

This is equivalent to the minimization of both polarization energies. Minimizing the latter quantity can be viewed as a least squares problem, for which an analytical solution exists. Indeed, rewriting it in a vectorial form we obtain

$$\min_{\mathbf{c}^i \in \mathbb{C}^{N_a}} f_{\text{obj}}(\mathbf{c}^i) = \min_{\mathbf{c}^i \in \mathbb{C}^{N_a}} \left(\mathbf{F}_v^i - \mathbf{B}_v^i \mathbf{c}^i\right)^{\mathrm{H}} \left(\mathbf{F}_v^i - \mathbf{B}_v^i \mathbf{c}^i\right) + \left(\mathbf{F}_h^i - \mathbf{B}_h^i \mathbf{c}^i\right)^{\mathrm{H}} \left(\mathbf{F}_h^i - \mathbf{B}_h^i \mathbf{c}^i\right) , \tag{3.8}$$

with H standing for the conjugate transpose. Equating its gradient to zero yields the following linear system of equations

$$\begin{pmatrix} \mathbf{B}_h^i \\ \mathbf{B}_v^i \end{pmatrix}^{\mathrm{H}} \begin{pmatrix} \mathbf{B}_h^i \\ \mathbf{B}_v^i \end{pmatrix} \mathbf{c}^i = \begin{pmatrix} \mathbf{B}_h^i \\ \mathbf{B}_v^i \end{pmatrix}^{\mathrm{H}} \begin{pmatrix} \mathbf{F}_h^i \\ \mathbf{F}_v^i \end{pmatrix} . \tag{3.9}$$

The latter equation has an unique solution if the columns of $\begin{pmatrix}\mathbf{B}_h^i \\ \mathbf{B}_v^i\end{pmatrix}$ are linearly independent. This is effectively the case in this problem and the left-hand side matrix is hence invertible, yielding the Moore-Penrose inverse. Equivalently, one can consider the following linear system of equations

$$\begin{pmatrix}\mathbf{B}_h^i \\ \mathbf{B}_v^i\end{pmatrix} \mathbf{c}^i = \begin{pmatrix}\mathbf{F}_h^i \\ \mathbf{F}_v^i\end{pmatrix}, \tag{3.10}$$

and solve it in the least-squares sense.

Nonetheless, the UAV device will not be able to capture those components since we make the assumption of a horizontal flight. Therefore, we project those components on the frame of reference. Indeed, in this chapter we do not take into account the UAV attitude and therefore we assume that at every moment of the flight, both UAV antennas are parallel to the array antennas. This yields

$$\begin{pmatrix}\mathbf{F}_x^i \\ \mathbf{F}_y^i\end{pmatrix} = \begin{pmatrix}\cos\theta\cos\varphi & -\sin\varphi \\ \cos\theta\sin\varphi & \cos\varphi\end{pmatrix} \begin{pmatrix}\mathbf{F}_v^i \\ \mathbf{F}_h^i\end{pmatrix} \tag{3.11}$$

where the angles are defined in Figure 3.1. We proceed analogously for $\mathbf{p}_v$ and $\mathbf{p}_h$.

In this expression we do not examine neither the r component (since it is zero) nor the z component (since we can not capture it).

3.1.1.2 Multiple coefficients per antenna

In this section the gain obtained by increasing the number of coefficients is evaluated. A possible way to proceed would be to use a coefficient for each MBF, or even a coefficient for each elementary basis function. However the number of variables rises quickly since the number of MBF is in the range of $20-40$ and each MBF is decomposed into 1218 basis functions. This yields $256^2 \times 40 = 2621440$ variables in the first case and more than 300 millions in the second case. This extremely huge number of calibration coefficients, in addition with the increasing computational complexity, may also not significantly improve the calibration. Therefore we decide to limit ourselves to the more dominant MBFs, the latter being classified by importance, we give one degree of freedom for the $N_{\mathrm{C,MBF}}-1$ first MBFs and a last one identical for the other ones, i.e. we have a tensor $\mathbf{c} \in \mathbb{C}^{N_a \times N_a \times N_{\mathrm{C,MBF}}}$. We easily rewrite (3.3),

$$\overline{\mathbf{F}_v^i} = \sum_{i_m=1}^{N_m} \sum_{i_a=1}^{N_a} cf_{i_m,i_a}^i \, \mathbf{p}_{v,i_m} \, e^{jk(x_{i_a}u_x + y_{i_a}u_y)} \, c_{i_a,i_m}^i , \tag{3.12}$$

$$= \sum_{i_a}^{N_a} \sum_{i_m=1}^{N_m} \mathbf{b}_{v,i_a,i_m}^i \, c_{i_a,i_m}^i = \mathbf{B}_v^i \, \mathbf{c}^i , \tag{3.13}$$

where in the last line we splitted both matrices into vectors, i.e. let i arbitrarily chosen, it yields for every $i_a = 1 \dots N_a$ and $i_m = 1 \dots N_m$

$$c^i_j := c^i_{i_a,i_m}\,, \tag{3.14}$$

$$B^i_{i_e,j} := B^i_{i_e,i_a,i_m} \qquad \forall i_e = 1 \dots N_e\,, \tag{3.15}$$

$$\Leftrightarrow j = N_a \times (i_m - 1) + i_a\,. \tag{3.16}$$

Finally we obtained the same problem as equation (3.4) with this time $\mathbf{c} \in \mathbb{C}^{(N_a \times N_{\mathrm{C,MBF}}) \times N_a}$ and $\mathbf{B}^i_v \in \mathbb{C}^{N_e \times (N_a \times N_{\mathrm{C,MBF}})}$. This yields an equivalent least-squares problem with normal equations (3.9).

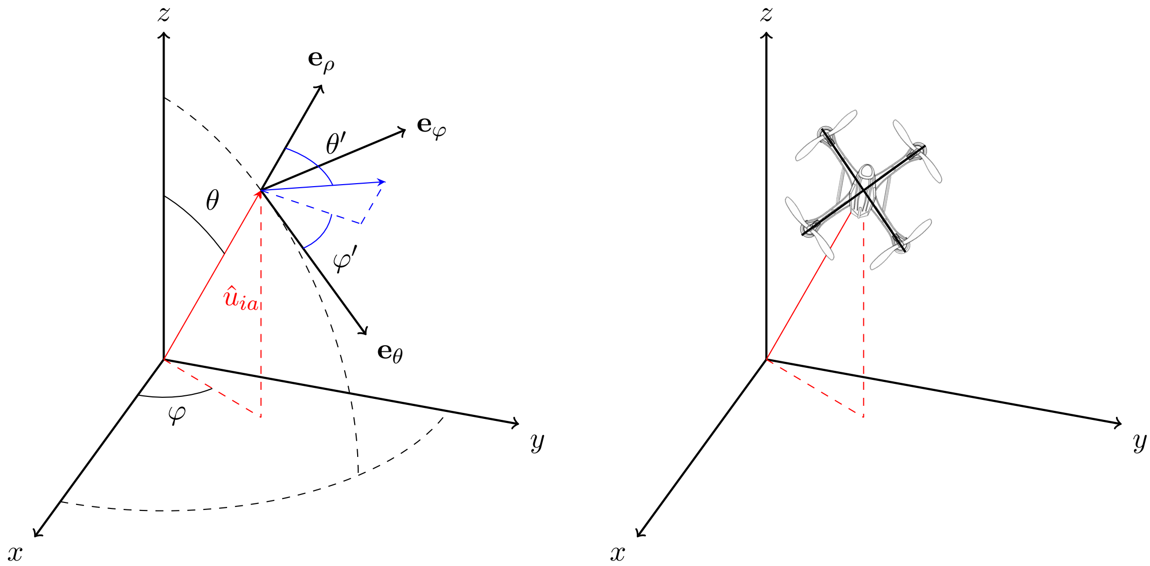

(A) Used coordinates. (B) Direction of UAV dipole antenna.

FIGURE 3.1: Sketch of the problem.

3.2 UAV flight strategy

In the context of a measurement campaign, a large number of parameters must be taken into account: on the transmitting side, the continuous-wave RF signal generator; the on-board Inertial Measurement Unit (IMU); the size, shape and component of the UAV itself; the Global Navigation Satellite System (GNSS) and on the receiving side, the RF receiver chain formed by the LNA, the analog RF-to-optical converter, etc. This list is non-exhaustive and some examples of real case test-systems can be found in [2, 3, 13]. Nevertheless, we focus in this discussion on the flight strategy and more specifically, on the drone path. We consider several path types:

1. spiral;
2. grid;

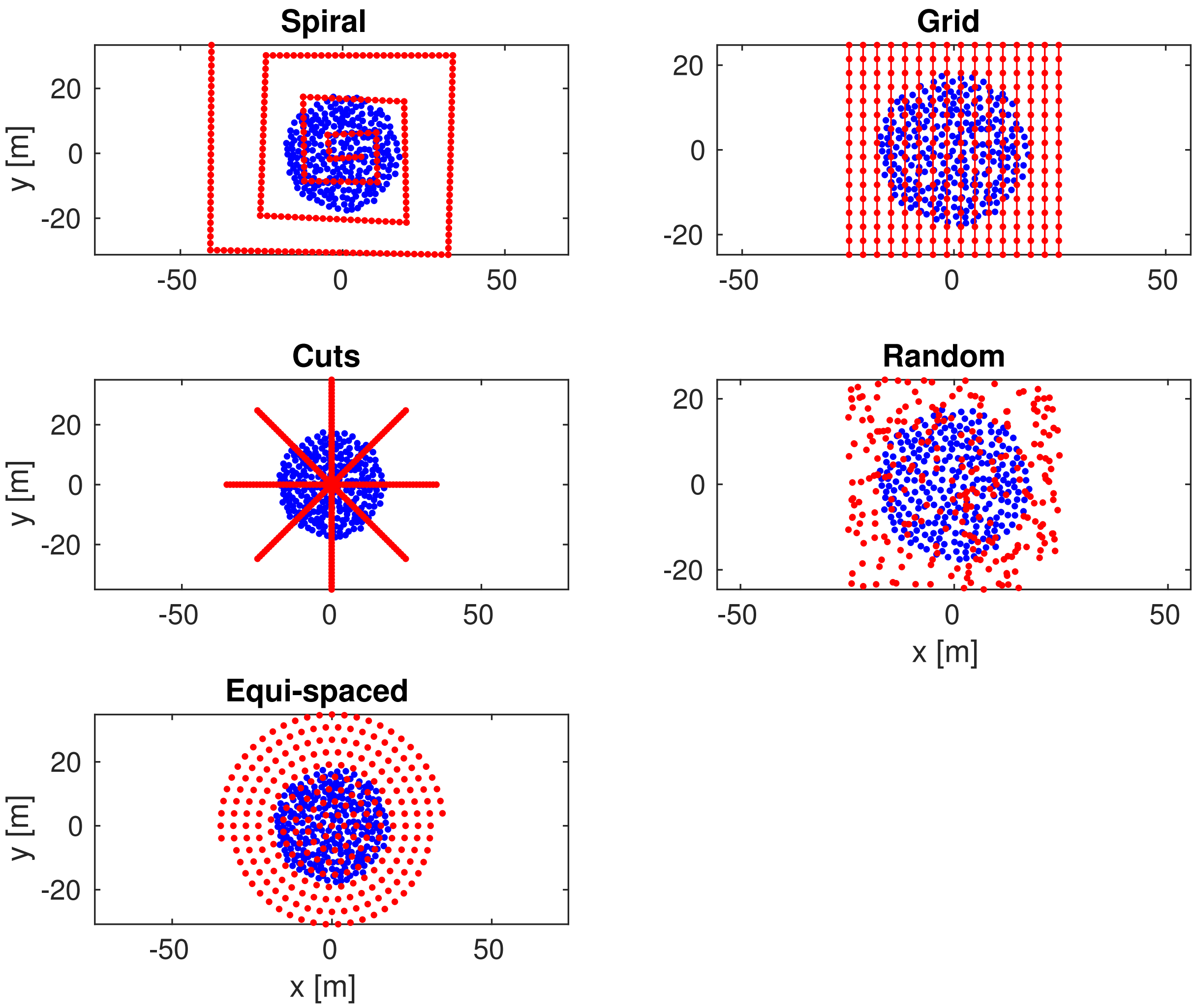

FIGURE 3.2: Studied UAV flight strategies with $2N_a$ experiment points. Spiral, grid and cuts scenarios are called direct because the UAV path between the points is directly seen. On the other hand, random and equi-spaced scenarios do not show an obvious structure.

3. cut;
4. random;
5. equi-spaced.

These types can be classified into 3 categories: direct single path (spiral, grid) where the UAV takes off, does all experiments and then lands on the ground; direct multiple path (cut) where the UAV performs several flights; and finally indirect paths (random, equi-spaced) where a cloud of point is examined instead of a concrete flight. These types are depicted in Figure 3.2. The flight strategies are obtained straightforwardly, except for the equi-spaced strategy: the spiral depends on the crossing-points, i.e. the edges; the grid, cuts and random depend on the maximal horizontal distance from array center, here taken as the diameter $D = 35\,\mathrm{m}$. Finally the last type needs further explanation.

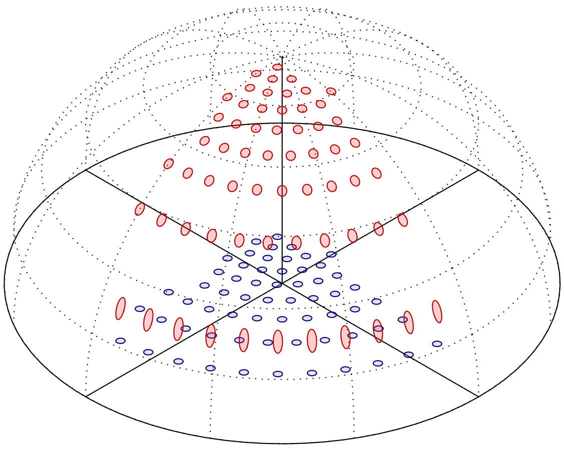

FIGURE 3.3: Projection of equi-spaced points (red) on a horizontal plan $z = \frac{R}{4}$ with R the sphere radius. For the sake of visibility, this figure shows only a quarter of the points.

Equi-spaced strategy. We proceed in the following way: first, we set a threshold θ_M and spread N_e points as uniformly as possible on the spherical cap defined by $\{(\theta, \varphi) \in [-\theta_M, \theta_M] \times [0, 2\pi]\}$[1]. These points are depicted in red in Figure 3.3. Then we project it onto the plane defined by the UAV height (h): $z = h$. Those points, depicted in blue in Figure 3.3, are our experiment points.

3.3 Results and discussions

In this section, the noise level used for the experiments is first defined. The error used to assess the performance of the method for different flight strategies is characterized. Afterwards, we describe the obtained results when there is no restriction on the flight time (Section 3.3.1) and when such a restriction is introduced (Section 3.3.2).

Noise level. In this chapter, we assume that the uncertainties only come from the UAV position. A random distribution centered around the true value is arbitrarily assumed with standard deviation $\sigma_m = 0.1\,\mathrm{m}$, meaning that there is no bias. Chapter 5 explores the attitude of the UAV and hence adds a new noise on the attitude.

Error definition. We inspect two main outcomes in order to judge the calibration quality: the whole array radiation pattern and the EEP. We define the error on these quantities as

$$e_{\theta,\varphi} = 10\log_{10}\left(\left|\mathbf{F}_v(\theta,\varphi) - \overline{\mathbf{F}_v(\theta,\varphi)}\right|^2 + \left|\mathbf{F}_h(\theta,\varphi) - \overline{\mathbf{F}_h(\theta,\varphi)}\right|^2\right) - 10\log_{10}\max_{\theta,\varphi}\left\{|\mathbf{F}_v(\theta,\varphi)|^2 + |\mathbf{F}_h(\theta,\varphi)|^2\right\}. \tag{3.17}$$

The maximum error e_M and the mean μ_e are also studied. As the maximum is taken over a finite number of points, the true maximum value may be higher. Nevertheless, one can show [23]

[1]This is an instance of the Tammes problem [22].

that the intensity of a circular radiator of radius r is given by

$$I(\theta) = I_0 \left(\frac{2J_1(kr\sin\theta)}{kr\sin\theta} \right)^2 = 4\, I_0\, \mathrm{Jinc}^2(x)$$

with J_1 the first-kind Bessel function and I_0 the maximum intensity. The Jinc function, also known as Sombrero function, has non-periodically spaced zeros [24] but the maxima are located in $\theta = m\pi$, $m \in \mathbb{Z}$. Since we interpolate this pattern using the grid $[\theta, \varphi] \in [-45 : 1 : 45] \times [0 : 1 : 360]$, we are far beyond the Nyquist critical frequency and we can assume that the maximum (after the relatively low-order interpolation done here) is close to the real one.

3.3.1 Array measurements far away from the array

Recall that we make here the assumption that there is no constraint on the UAV max flight time. Hence, it can hover as far as desired. Please note that this assumption is very strong. Indeed, due to the far-fied condition, we need to fly very high (1 km for a frequency of 140 MHz). This implies that one needs to fly far away from the antenna array in order to capture the sidelobes. For instance, if experiment points at zenith angle $\theta = 60°$ are needed, basic trigonometry gives that we should fly 1700 m away from the array center. The author is well aware that such a flight plan is unlikely to be achieved by a UAV. Yet, it gives a lower bounds on the errors.

The error $e_{\theta,\varphi}$ on the whole AP is shown in Figure 3.4. We see that every flight strategy, except the one using cuts, estimates correctly the array pattern. This is mainly due to the poor distribution of measurements in this strategy. The equi-spaced strategy seems to give the best results, while the spiral strategy lags behind. These visual observations are confirmed by the maximum and mean errors gathered in Table 3.1. We observe that the four best flight strategies provide similar error values (up to 4 dB of difference). Hence, with the aforementioned strong assumption, very good accordance between expected and estimated pattern is obtained.

Flight strategy	e_M (dB)	μ_e (dB)
Spiral	-60.9	-74
Grid	-63.4	-75.5
Cuts	-29.8	-45.3
Random	-60	-74.3
Equi-spaced	-64.3	-76.5

Table 3.1: Errors with measurements far away from the array. Experiment taken at 1000 m height with $\sigma_m = 0.1$ m and points taken up to 1500 m far from array center.

3.3.2 Array measurements close to the array

The assumption about the flight time restriction made in the previous section is now removed. We restrict the flight time and prevent the UAV from flying more than 200 m away from the

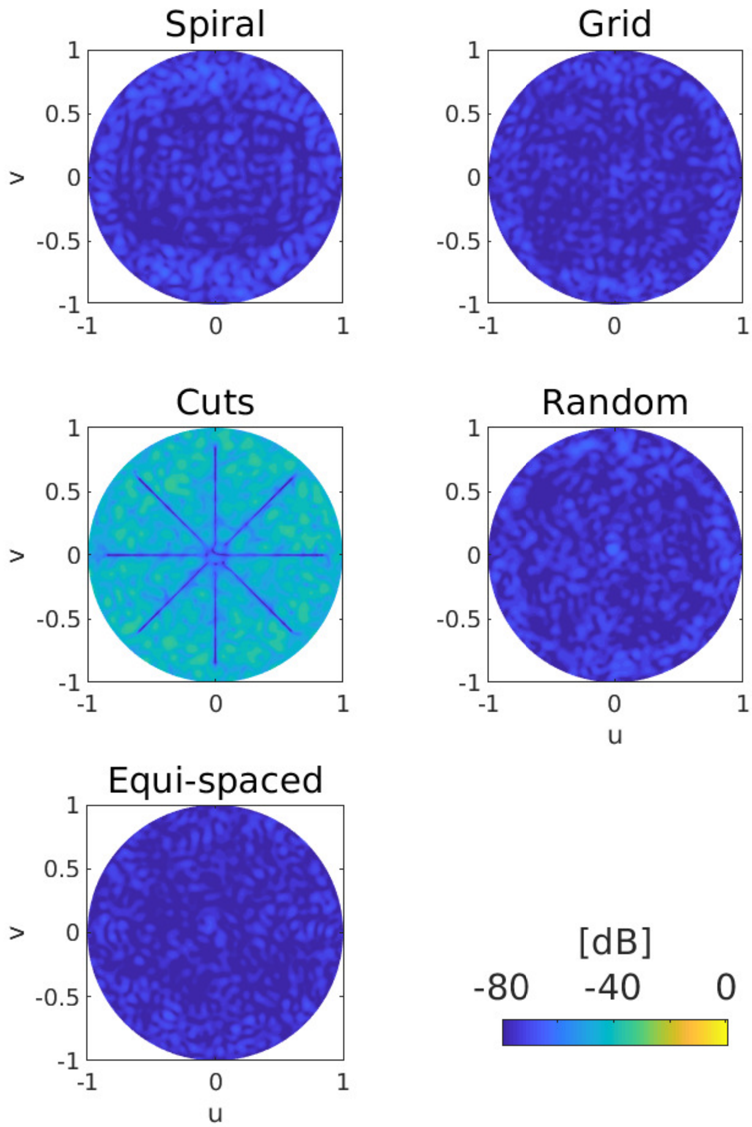

FIGURE 3.4: Error pattern $e_{\theta,\varphi}$ with several far-field flight strategies covering the whole array pattern. Experiments are taken at 140 MHz and altitude 1000 m with noise level $\sigma_m = 0.1$ m.

array center. Figure 3.5 shows the error $e_{\theta,\varphi}$ on the whole array pattern. We see that every flight strategy correctly estimates the array pattern on its specific path but that the error explodes everywhere else. The calibration output is clearly not acceptable. This is typically due to the condition number of matrices $\mathbf{B}^i$, i.e. the ratio of the maximum to the minimum singular value, which increases up to 10^{12} in that case: from the array point of view, the data are highly redundant in a small part of the whole pattern and are completely missing in a large part (e.g. sidelobes).

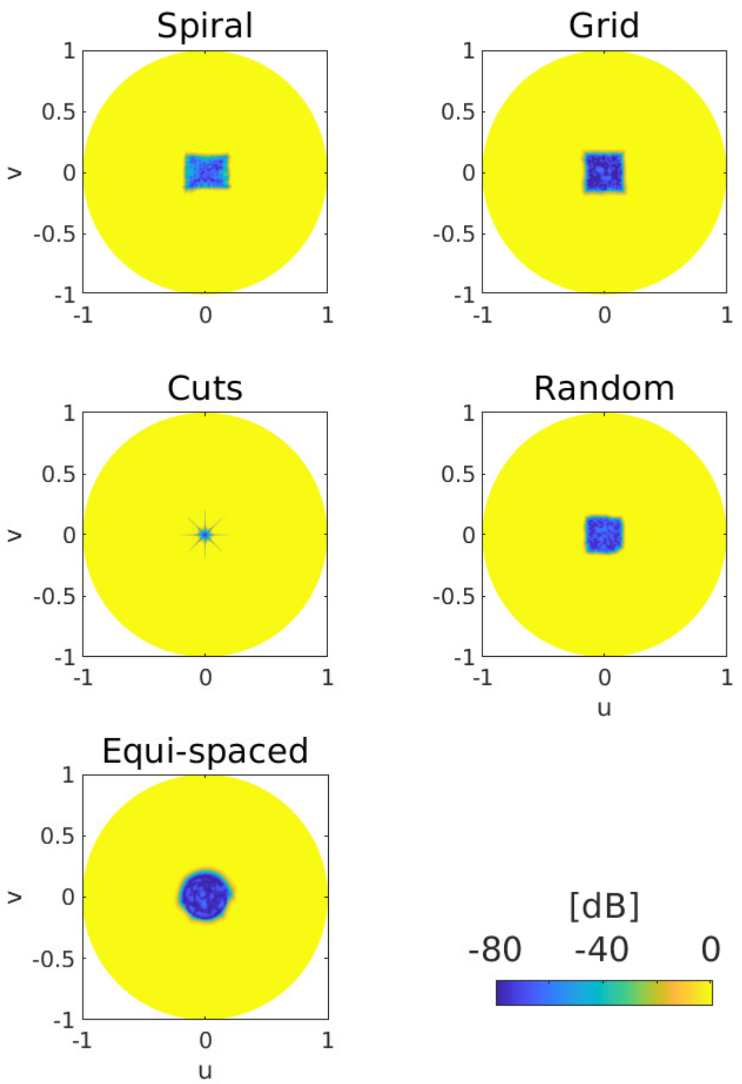

FIGURE 3.5: Error pattern $e_{\theta,\varphi}$ with several far-field flight strategies not covering the whole array pattern. Experiments are taken at 140 MHz at an altitude of 1000 m with a noise level of $\sigma_m = 0.1$ m.

3.3.3 Impact of the noise level

Under the assumption according to which the flight time is not restricted, the relationship between the noise level and the error is linear in a logarithmic scale; see Figure 3.6. This relationship is linear given that the relative position error with respect to the height is very small, leading to small errors on the direction angles θ and φ. Also, the MBF patterns $\mathbf{p}$ are not computed exactly at the directions of interest, they are in fact interpolated from a precomputed grid of points. This interpolation relies on cosines and sines. Hence, for small angle perturbation, linear behaviour is observed. This is not the case when the relative error increases, e.g. if the altitude decreases (see Chapter 4).

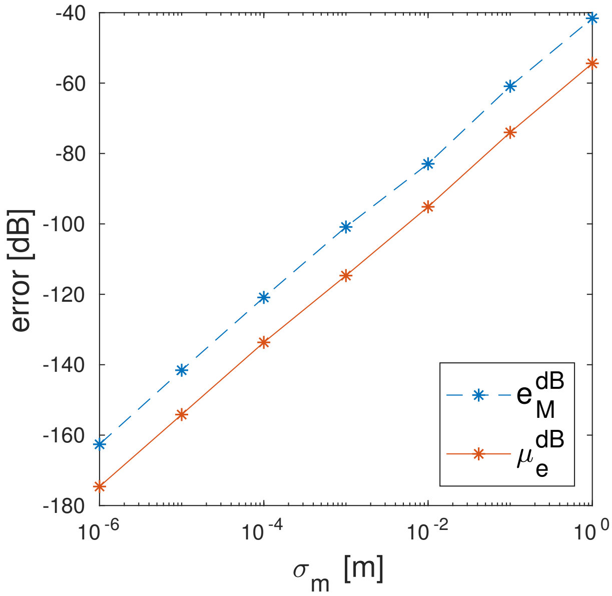

FIGURE 3.6: Error as a function of the noise level on the position.

3.4 Conclusion

In this chapter, a calibration with a UAV flying in the far field has been studied. We have first shown how this problem can be formulated in the least-squares sense (for one coefficient and multiple coefficients per antenna). The described method has been tested for various flight strategies.

The calibration outcomes appear to be very satisfactory when we assume that there is no restriction on the UAV flight time. However, in practice, this assumption cannot be made. When we remove it, the estimated AP increases too much in region when no data are available. This phenomenon of an analysis corresponding too closely to a particular set of data is known as *overfitting*. This issue will be handled in Chapter 6.

Finally, a last remark concerning the fact that no results with multiple coefficients are presented: increasing the number of coefficients does not improve the calibration. The obtained error levels from our experiments are similar with slightly better outcomes in the case of a single coefficient. It is due to an oversizing of the number of variables and also to the fact that the reference solution is assumed to have the same calibration coefficients for each MBF. Yet, this multiple coefficients approach may be useful when considering additional elements to the model, e.g. the finite ground plane effects.

Chapter 4

Near-field calibration

Some UAV have already been operating at altitudes higher than 3 km, which is the Fraunhofer distance at 350 MHz [25], making the far-field calibration technically possible. However, a calibration at that altitude has several disadvantages. Firstly, the signal-to-noise ratio (SNR), which is not considered in this work, will certainly decrease with increasing distance. Secondly, at that altitude and in order to reach a given station, the pulse sent by the UAV may badly interfere with the other stations. Indeed, as explained in the introduction, the SKA-low will consist among others in a core of closely spaced stations. It is therefore not wanted that the calibration of a single core station forces the interruption of a number of stations. Moreover the flight time is a scarce resource and we showed that, for an efficient far-field calibration, we need to capture the sidelobes which are very far away from the array center.

As a consequence, it may be interesting to analyze a calibration scenario when flying a lot closer to the array. Nonetheless, we want to stay far enough in order to still satisfy the far-field condition *with respect to the antenna.* Considering here the SKALA with footprint of $1.2 \times 1.2\,\mathrm{m}^2$ and height 1.8 m [16, 26] we should hover at a minimum distance of 4 m for the highest frequency. Hence a device hovering at 10 m will be in the near field with respect to the array but in the far field with respect to the antennas.

In this chapter we first explain how, using HARP, the fields can be expressed at that distance from the array. Results are shown in Section 4.1.1 for various path types and numbers of measurements. Impacts of the maximal distance and of the number of measurements are discussed.

4.1 Method

As before, the calibration is performed using the exact measurements on perturbed positions. The near-field case is in apparency quite different from the previous chapter. However, some algebraic transformations will lead us to an analogous formulation. The MBF-patterns are firstly calculated over a whole sphere. They are then represented using spherical wave expansions. Finally, the evaluation of the fields in a specific direction is realized by interpolating (using angle and distance) these patterns.

Assuming now that the pattern of each ON-antenna i can be computed, we need to combine these pattern values at position i_e defined by (x_e, y_e, z_e). In this case, the electric field cannot be as easily defined by Ludwig II definition [21]. Indeed, the unit vector of the polarizations is angle-dependent, and for near field, the angle from each antenna to the observation point is different. Thus, we first express the field from each antenna using Ludwig II definition and then, we transform it into Ludwig I definition, i.e. with respect to the inertial directions x, y and z. Doing so, the total fields are computed by summing up every antenna contribution

$$\begin{pmatrix} E^i_{x,i_e} \\ E^i_{y,i_e} \end{pmatrix} = \sum_{i_a=1}^{N_a} \sum_{i_m=1}^{N_m} \underbrace{\begin{pmatrix} \cos\theta_{i_e,i_a}\cos\varphi_{i_e,i_a} & -\sin\varphi_{i_e,i_a} \\ \cos\theta_{i_e,i_a}\sin\varphi_{i_e,i_a} & \cos\varphi_{i_e,i_a} \end{pmatrix}}_{:=U_{i_e,i_a}} \begin{pmatrix} E^{i_m}_{v,i_e,i_a} \\ E^{i_m}_{h,i_e,i_a} \end{pmatrix} cf^i_{i_m,i_a} \tag{4.1}$$

$$= \sum_{i_a=1}^{N_a} U_{i_e,i_a} \begin{pmatrix} \mathbf{E}_{v,i_e,i_a} \cdot \mathbf{cf}^i_{i_a} \\ \mathbf{E}_{h,i_e,i_a} \cdot \mathbf{cf}^i_{i_a} \end{pmatrix} \tag{4.2}$$

where E^i_{x,i_e} is the x component of the electrical field at position (x_e, y_e, z_e) of the antenna under test (AUT) EEP, $\mathbf{E}_{v,i_e,i_a}$ a $\mathbb{C}^{N_m}$ vector containing the interpolation of the MBF-patterns of antenna i_a at position (x_e, y_e, z_e) viewed by this specific antenna and $cf^i_{i_a,i_m}$ is the coefficient, computed by HARP, of the i_m-th MBF of antenna i_a when only antenna i is ON. The angles θ_{i_e,i_a} and φ_{i_e,i_a} are defined by the relative position of the UAV (x_e, y_e, z_e) with respect to antenna i_a. Adding a coefficient for each antenna and proceding for every experiment point i_e leads to a formula totally analogous to equation (3.4). The x component reads

$$\mathbf{E}^i_x = \sum_{i_a=1}^{N_a} \mathbf{b}^{x,i}_{i_a} c^i_{i_a} = \mathbf{B}^{x,i}\mathbf{c}^i \,, \tag{4.3}$$

where $\mathbf{b}^{x,i}_{i_a}$ is a column of $\mathbf{B}^{x,i}$, defined by

$$B^{x,i}_{i_e,i_a} = \begin{pmatrix} \cos\theta_{i_e,i_a}\cos\varphi_{i_e,i_a} & -\sin\varphi_{i_e,i_a} \end{pmatrix} \begin{pmatrix} \mathbf{E}_{v,i_e,i_a} \cdot \mathbf{cf}^i_{i_a} \\ \mathbf{E}_{h,i_e,i_a} \cdot \mathbf{cf}^i_{i_a} \end{pmatrix} . \tag{4.4}$$

In these expressions, $\mathbf{B}^i_v \in \mathbb{C}^{N_e \times N_a}$ contains the contributions of every antenna i_a to each experiment point i_e, as computed by HARP using the noisy positions. Similarly to the far-field case, the UAV device is assumed to perform a flight horizontally, and the z component cannot be captured. Minimizing the energy of both components leads to a linear system of equations similar to (3.9)

Once the calibration coefficients **c** are found, we are able to compute the *far-field* radiation pattern using HARP. Indeed the goal remains to estimate as closely as possible the far-field patterns: for both the EEP and the whole array pattern. In this discussion, since real measurements are not available, we compare on one hand the far-field pattern with unperturbed data and on the other hand the computed pattern with perturbed data. One should note that, due to the non-capture of the z component, the received field level for the vertical polarization decreases while θ increases and the SNR becomes worse.

4.1.1 Results and discussion

The main parameter taken into account in this thesis is the UAV flight strategy. As explained previously, the flight time is a scarce resource and a well-designed path is preferable. In this section we evaluate the same five flight strategies as above. Experiments have been performed with a noise level on positions equals to $\sigma_m = 5\,\mathrm{cm}$.

4.1.1.1 Impact of the UAV path types

We observe in Figure 4.1 that the calibration outcomes with short drone paths are more satisfying than in the far-field case; compare with Figure 3.5. Indeed, the problem is naturally well-posed for all flight strategies, except for the one using cuts. Hence the overfitting phenomenon is drastically reduced. However, the maximum and mean error (Table 4.1) are approximately 30 dB higher than with the far-field calibration over the whole array (Table 3.1). This is due to a better distribution of the data points in the sidelobes for the latter case. Recall that this error is taken with respect to the main beam level and we already have at least 20 dB of difference between main and first sidelobes. One should take care that, even at $-30\,\mathrm{dB}$, the sidelobes are not contaminated by the noise. This can be done by comparing the reference and calibrated normalized array patterns with the absolute difference between their non-normalized versions. Figure 4.2 depicts two cuts of the AP for a spiral path. We observe that the pattern is satisfactorily estimated until the second sidelobes. This is not the case anymore beyond. Calibration will be enhanced below by increasing the number of experiments.

Flight strategy	e_M (dB)	μ_e (dB)
Spiral	-31.1	-41.3
Grid	-31.72	-42.5
Cuts	-20.6	-31.2
Random	-28.7	-41.0
Equi-spaced	-29.7	-41.1

TABLE 4.1: Errors with measurements close to the array. Experiments taken at 10 m height with $\sigma_m = 0.05\,\mathrm{m}$ and points taken up to 25 m far from array center.

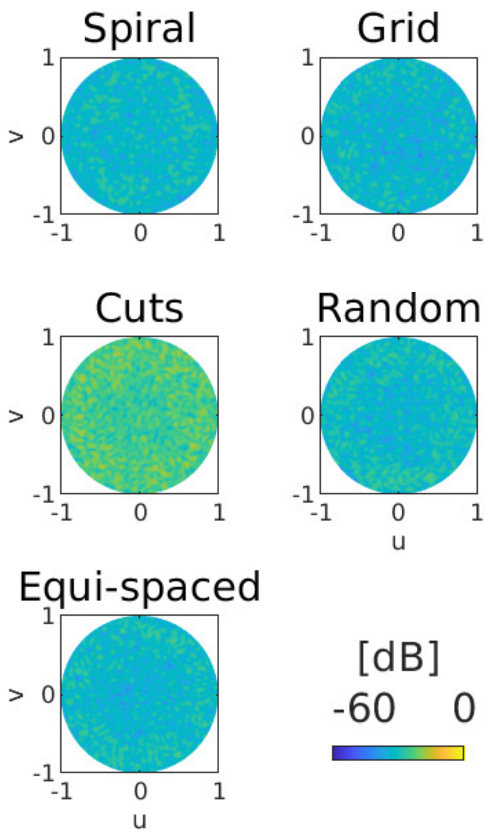

FIGURE 4.1: Error pattern $e_{\theta,\varphi}$ for several near-field flight strategies. N_a experiments are taken at 140 MHz at an altitude of 10 m with a noise level $\sigma_m = 0.05$ m.

4.1.1.2 Trade-off in maximal distance

In the FF case, the situation is straightforward: each data point contributes to increase our knowledge of the array pattern in a given direction. This is not the case anymore in a NF calibration: here, every antenna observes the data points with different directions. Therefore, an equi-spaced strategy does not give the best outcome anymore. It is optimal with respect to the antennas in the center of the array, but not at all for antennas at the boundary. On the other hand, if we make sure to select points optimally for every antenna, then a lot of points are not useful for some antennas since located too far in the sidelobes. This situation is depicted in Figure 4.4: we observe that the data point P is useful for antenna A, since it is located at $\theta = 45°$. However, antenna B sees P at $\theta \approx 72°$ which is beyond the scope of interest. There is therefore a trade-off about how far we allow the UAV to fly away from the array center. This trade-off is illustrated in Figure 4.5. We find an optimal distance of approximately 30 m.

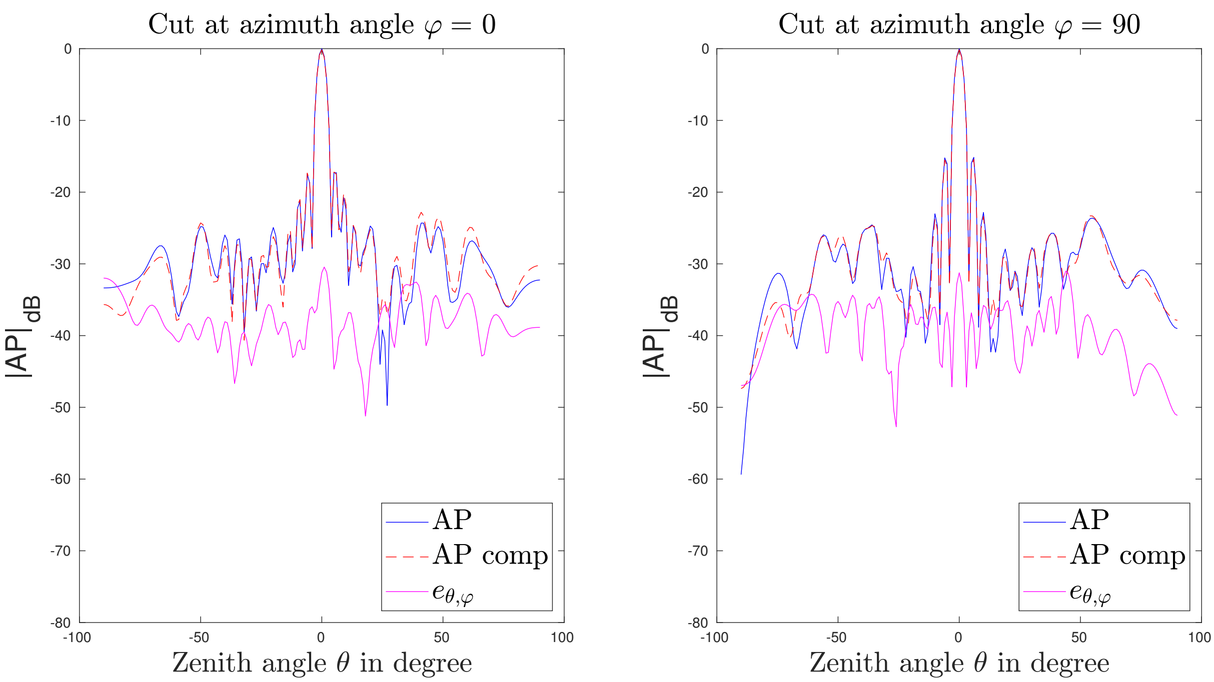

FIGURE 4.2: Discrepancies between reference and computed, i.e. calibrated, array pattern for NF spiral strategy with same parameters as Table 4.1.

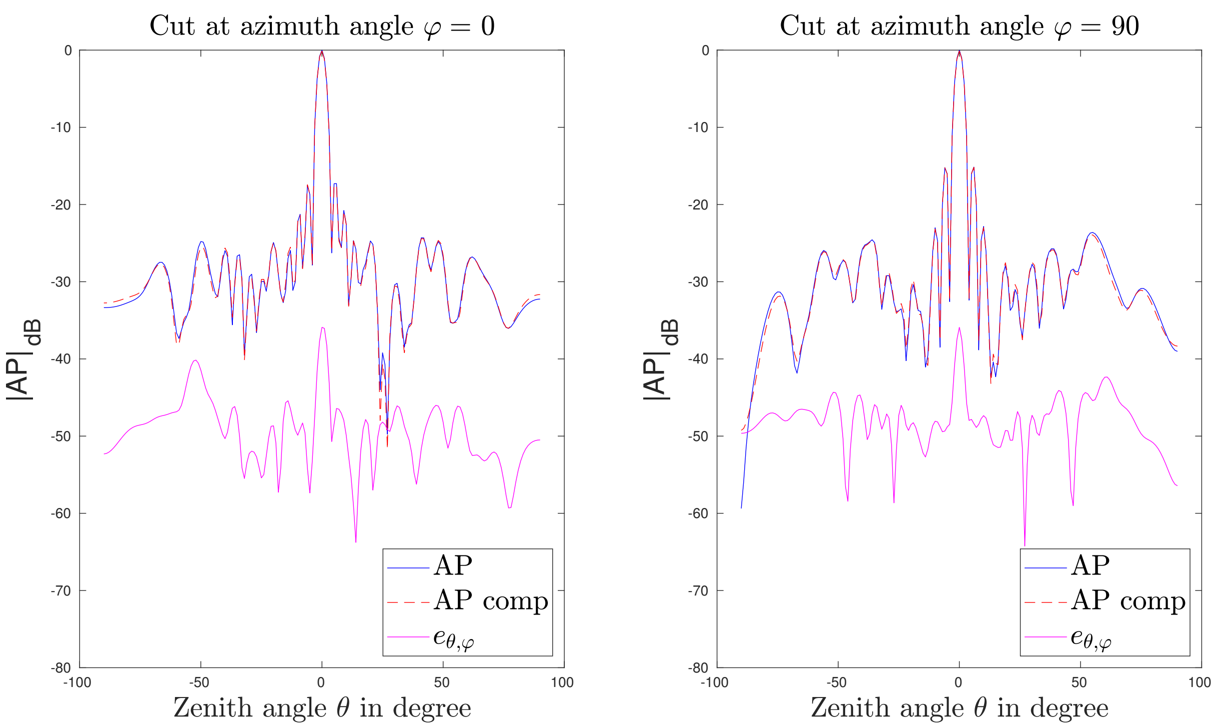

FIGURE 4.3: Discrepancies between reference and computed, i.e. calibrated, array pattern for NF spiral strategy with same parameters as Figure 4.2 except the number of experiments: $8N_a$.

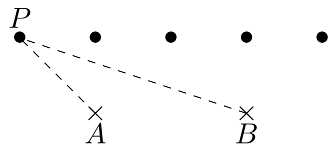

FIGURE 4.4: Sketch of a situation where some data points are not useful for every antenna. Here × stands for an antenna and • for a data point.

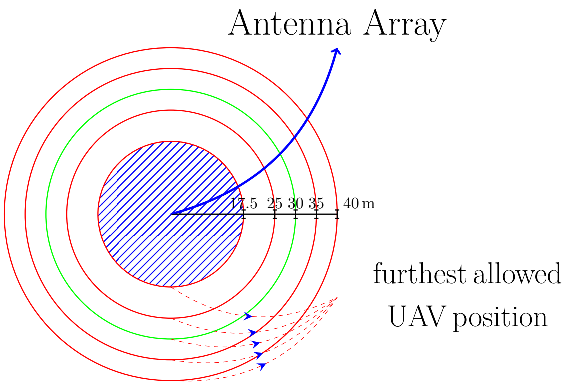

(A) Furthest allowed UAV position, we restrict it due to battery-time concerns.

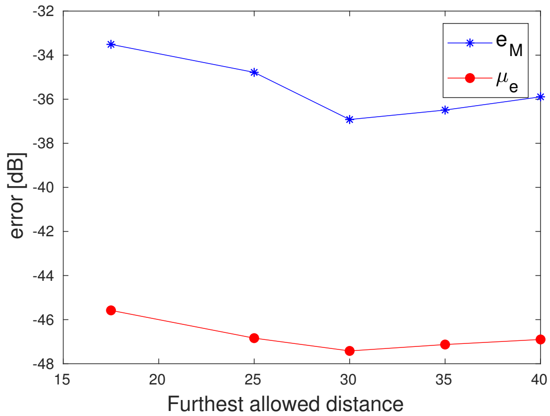

(B) Comparison of error with equi-spaced flight strategy with several max distance allowed.

FIGURE 4.5: Illustration of the trade-off between a flight close to the array center, unable to capture the sidelobes antennas at the boundary, and a flight far from the array center, where a lot of points do not contribute to the calibration. The optimum of these 5 points is 30 m and is depicted in green.

4.1.1.3 Impact of the number of measurements

Recall, that for each pulse sent by the drone, an *experiment*, we collect a current *measurement* on every antenna. Besides, the calibration coefficients offer us in the case of a single coefficient per antenna $N_a \times N_a$ degrees of freedom. In order to obtain a well-posed system of equations, we need $N_a \times N_a$ measurements and thus N_a experiments. Nevertheless one can also have more measurements than unknowns leading to a system of equations which we can solve in the least-squares sense. This idea of over-determining the system allows us to smooth the effect of the noise. One can observe the outcomes for several number of measurements in Figure 4.6. We see that flight types 1, 2, 4, 5 follow the same pattern while type 3, the cut strategy, is less sensitive. We observe that the maximum error decreases slower that the mean error. Besides, the cuts strategy appears to be quickly limited. This suggests either to increase the number of cuts or to pick an other strategy.

4.1.1.4 EEP estimate

Figure 4.7 shows the computed EEP of a single antenna. The error is more flat than for the AP; compare the cuts in Figure 4.3 with Figure 4.8.

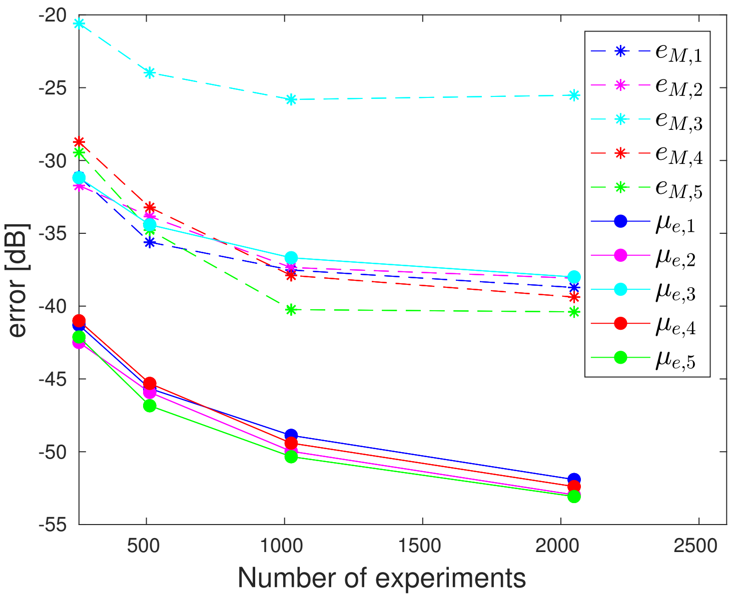

FIGURE 4.6: Comparison of the evolution of the errors with respect to the number of experiments for different flight strategies. Here $e_{M,i}$ stands for the max error and $\mu_{e,i}$ stands for the mean error of flight type i.

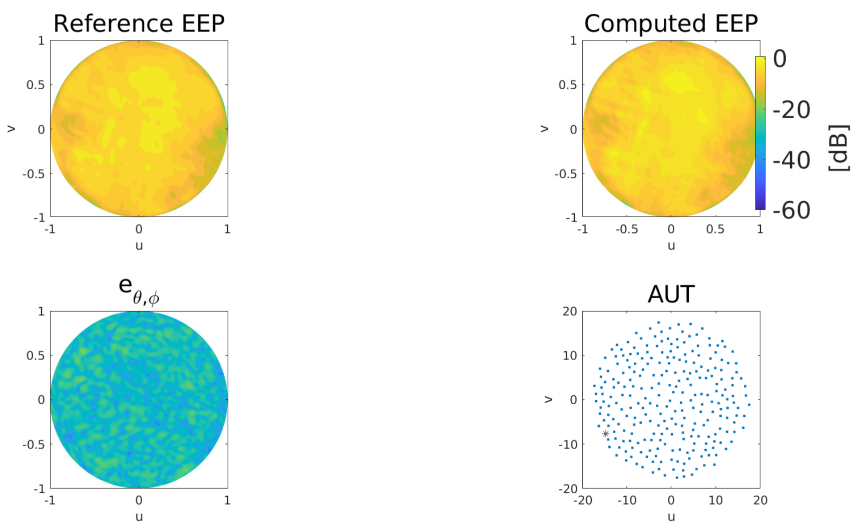

FIGURE 4.7: Reference, calibrated and error embedded element pattern. Simulation obtained with 1024 experiments with FF spiral flight strategy. The AUT is depicted in red in the bottom right figure.

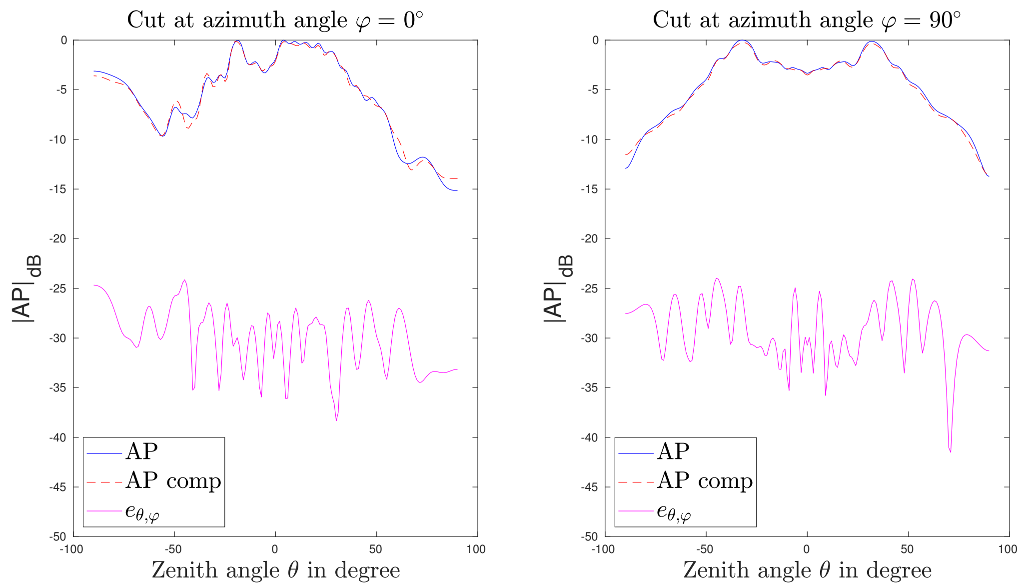

FIGURE 4.8: Error pattern cuts. Simulation obtained with 1024 experiments with FF spiral flight strategy. The AUT is depicted in red in the bottom right figure in Figure 4.7.

4.2 Conclusion

In this chapter, a near-field calibration has been presented. It differs from the FF case in the following points: the altitude is drastically reduced, which implies that the travel distance needed to cover the whole array with the UAV is smaller. For instance, while a distance of 1.7 km must be traveled to reach the sidelobes at $\theta = 60°$, here this distance is reduced to 17 m which is much more feasible in practice. Secondly, the number of experiments necessary for a given accuracy is larger in the NF case.

We first showed that the NF problem can be expressed similarly to the FF one, leading to a least squares problem. Regarding the results compared to the FF case, no overfitting phenomenon is observed for most flight strategies. It is still slightly present for the cuts strategy. However, we find that the overall error with 256 experiments is not acceptable. Increasing the number of experiments remedy this issue and leads to an error improvement of approximately 15 dB, with a final average error down to -52 dB.

Chapter 5

Modelling the UAV reception

In the previous chapter, we made the hypothesis that the UAV remains perfectly parallel to antennas and therefore that the x and y components are captured. Unfortunately, this hypothesis may be too strong from a realistic point of view. The attitude of the UAV should be taken into account, which leads to a mix between both components. This model extension of the UAV reception[1] is described in the present chapter.

5.1 Method

The derivation is made for a single observation point $\mathbf{P}$. Hence, vectorial notation is used here for horizontal and vertical polarization, following Ludwig II definition. We compute the electric field due to the ON-antenna i at distance R_i via its embedded element pattern $\mathbf{F}^i$ as,

$$\mathbf{E}^i = \mathbf{F}^i \, \frac{e^{-jkR_i}}{R_i} V_i^t \,, \tag{5.1}$$

where V_i^t is the voltage applied on the antenna. This equation does not follow the IEEE convention where the antenna is excited by an unitary current source. Using a voltage source with appropriate series impedance Z_L (from the Thevenin equivalent circuit) leads to more compact expressions since no impedance mismatch factor appears. Therefore the received voltage on UAV antenna $k \in \{1, 2\}$ at observation point $\mathbf{P} := \overline{O_A O_D}$ and the distance R_i of the AUT i is

$$V_{i,k}^r = \frac{2\lambda Z_L}{j\eta} \mathbf{F}_k^d \cdot \mathbf{F}^i \frac{e^{-jkR_i}}{R_i} V_i^t \,, \tag{5.2}$$

[1]The reader should keep in mind the use of the reciprocity. Indeed, the UAV is the physical transmitter and the antenna is the physical receiver. Nevertheless, it is mathematically more convenient – and equally accurate – to consider the converse.

where $\mathbf{F}_k^d$ stands for the radiation pattern of drone antenna k. Summing up the contribution of every array antenna, we obtain the total voltage on UAV antenna k,

$$V_k^r = \sum_{i=1}^{N_a} V_{i,k}^r \, . \tag{5.3}$$

Now by using the same MBF framework as in equation (3.1), we decompose the EEP. This yields

$$V_k^r = \sum_{i=1}^{N_a} \frac{2\lambda Z_L}{j\eta} \sum_{i_m=1}^{N_m} \sum_{i_a=1}^{N_a} \underbrace{\mathbf{F}_k^d(\hat{u}_{ia}, \Omega) \cdot \mathbf{p}_{i_m}(\hat{u}_{ia})}_{\text{scal. prod.}} \, cf_{i_m,i_a}^i \frac{e^{-jkR_{ia}}}{R_{ia}} V_i^t \, , \tag{5.4}$$

where $\hat{u}_{ia}$ is the unit vector pointing from the antenna i_a to the UAV and Ω the three angles describing the UAV attitude. This last expression, as complicated as it may seem at first glance, exhibits the same structure as equation (3.3) and can be simplified in a way similar to equation (3.4). Nevertheless, we should investigate how to compute the scalar product appearing in equation (5.4). This is the purpose of the next section.

5.1.1 Computation of the scalar product

This problem can be addressed by considering 4 different systems of coordinates: the first one is set at the transmitting antenna, the second one is a mobile spherical system of coordinates, the third one is the local mobile system of the drone and the last one corresponds to the mobile spherical system referenced to the third one. The geometry is sketched in Figure 5.2. One can observe that, since we assume to be in the far field with respect to the single considered array antenna and with respect to the UAV antenna, both radiation patterns exhibit a spherical wave behaviour and therefore belong to the same plane orthogonal to $\mathbf{e}_{\rho'} = -\mathbf{e}_\rho$. Hence, the scalar product between patterns is only determined by the angle between $\mathbf{e}_\theta$ and $\mathbf{e}_{\theta'}$. In order to compute this scalar product, we are going to express every vector in the inertial system (x, y, z).

Expression of $\mathbf{e}_\theta$ and $\mathbf{e}_\varphi$. We simply rotate the second system of coordinates by using the unitary matrix

$$U(\theta, \varphi) = \begin{pmatrix} \sin\theta\cos\varphi & \sin\theta\sin\varphi & \cos\theta \\ \cos\theta\cos\varphi & \cos\theta\sin\varphi & -\sin\theta \\ -\sin\varphi & \cos\varphi & 0 \end{pmatrix} , \tag{5.5}$$

which leads to the following equation

$$\begin{pmatrix} \mathbf{e}_\rho \\ \mathbf{e}_\theta \\ \mathbf{e}_\varphi \end{pmatrix} = U(\theta, \varphi) \begin{pmatrix} \hat{\mathbf{x}} \\ \hat{\mathbf{y}} \\ \hat{\mathbf{z}} \end{pmatrix} . \tag{5.6}$$

Since we are not interested in $\mathbf{e}_\rho$, we define U_2 as the matrix U from which the first line has been removed.

Expression of $\mathbf{e}_{\theta'}$ and $\mathbf{e}_{\varphi'}$. Similarly to the previous section,

$$\begin{pmatrix} \mathbf{e}'_\rho \\ \mathbf{e}'_\theta \\ \mathbf{e}'_\varphi \end{pmatrix} = U(\theta', \varphi') \begin{pmatrix} \hat{\mathbf{x}}' \\ \hat{\mathbf{y}}' \\ \hat{\mathbf{z}}' \end{pmatrix} = U(\theta', \varphi') T(\alpha, \beta, \gamma) \begin{pmatrix} \hat{\mathbf{x}} \\ \hat{\mathbf{y}} \\ \hat{\mathbf{z}} \end{pmatrix}, \tag{5.7}$$

where T is the composition of the three elemental rotation matrices allowing us to move from the antenna coordinates system (CS) to the UAV one. Using proper TAIT-BRYAN's angle (α, β, γ) (yaw, pitch and roll : Figure 5.1) with $(Z-Y-X)$ *intrinsic* rotations [27] and defining $c_\alpha = \cos\alpha$ and $s_\alpha = \sin\alpha$ one can show that

$$T(\alpha, \beta, \gamma) = \begin{pmatrix} c_\alpha c_\beta & c_\alpha s_\beta s_\gamma - c_\gamma s_\alpha & s_\alpha s_\gamma + c_\alpha c_\gamma s_\beta \\ c_\beta s_\alpha & c_\alpha c_\gamma + s_\alpha s_\beta s_\gamma & c_\gamma s_\alpha s_\beta - c_\alpha s_\gamma \\ -s_\beta & c_\beta s_\gamma & c_\beta c_\gamma \end{pmatrix}. \tag{5.8}$$

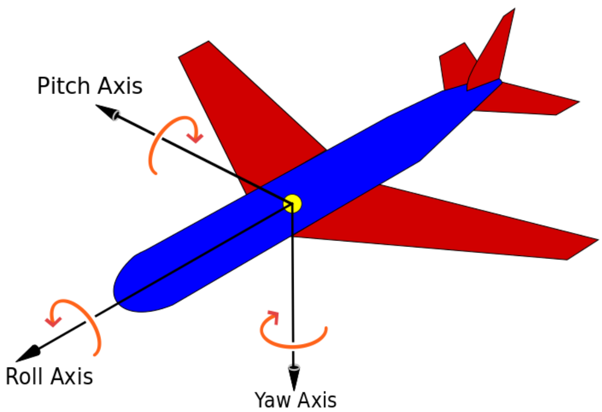

FIGURE 5.1: TAIT-BRYAN's angles used to model UAV attitude. Wikipedia - Euler's Angles.

Computation of the projection. Finally, we are only interested in the projection of these elementary vectors. Hence, we can compute the projection matrix P

$$P := \begin{pmatrix} \mathbf{e}_\theta \cdot \mathbf{e}'_\theta & \mathbf{e}_\theta \cdot \mathbf{e}'_\varphi \\ \mathbf{e}_\varphi \cdot \mathbf{e}'_\theta & \mathbf{e}_\varphi \cdot \mathbf{e}'_\varphi \end{pmatrix} = \begin{pmatrix} \mathbf{e}_\theta \\ \mathbf{e}_\varphi \end{pmatrix} \begin{pmatrix} \mathbf{e}'_\theta & \mathbf{e}'_\varphi \end{pmatrix}, \tag{5.9}$$

$$= U_2(\theta, \varphi) T^t(\alpha, \beta, \gamma) U_2^t(\theta', \varphi'). \tag{5.10}$$

The scalar product in equation (5.4) can be expressed as

$$\mathbf{F}^d(\hat{u}_{ia}, \Omega) \cdot \mathbf{p}_{i_m}(\hat{u}_{ia}) = \begin{pmatrix} F^d_{\theta'} & F^d_{\varphi'} \end{pmatrix} \begin{pmatrix} \mathbf{e}_{\theta'} \\ \mathbf{e}_{\varphi'} \end{pmatrix} \begin{pmatrix} \mathbf{e}_{\theta} & \mathbf{e}_{\varphi} \end{pmatrix} \begin{pmatrix} p^{\theta}_{i_m} \\ p^{\varphi}_{i_m} \end{pmatrix} , \tag{5.11}$$

$$= \begin{pmatrix} F^d_{\theta'} & F^d_{\varphi'} \end{pmatrix} P^t \begin{pmatrix} p^{\theta}_{i_m} \\ p^{\varphi}_{i_m} \end{pmatrix} . \tag{5.12}$$

This last equation is almost totally determined: since the attitude of the drone is assumed to be known (α, β, γ) and (θ, φ) are data of the measurements. However, one needs to investigate how to recover (θ', φ') from the former data.

Computation of (θ', φ'). Using the aforementioned linear transformations we express the observation point O_D in $(\hat{\mathbf{x}}', \hat{\mathbf{y}}', \hat{\mathbf{z}}')$ via T :

$$\begin{pmatrix} x_D \\ y_D \\ z_D \end{pmatrix} = -T^{-1}(\alpha, \beta, \gamma) \begin{pmatrix} x'_D \\ y'_D \\ z'_D \end{pmatrix} . \tag{5.13}$$

The minus comes from the fact that the point in the inertial frame of reference is opposite to the same point in the mobile frame. Finally, using the spherical mapping we obtain the desired angles.

5.1.2 UAV pattern model

The UAV is modelled with two orthogonally mounted antennas. The model is quite approximate: the mesh is given in Figure 5.3 and consists in a rectangular plate with the two antenna arms. The output pattern is given in Figure 5.4. The behaviour of an actual UAV pattern is expected to be similar, as long as the whole structure is smaller than half the wavelength. For the actual implementation of such a system, a more accurate UAV modelling or even better, measurements carried out in anaechoic chamber, should be investigated. In order to obtain the UAV pattern in a specific (θ, φ) direction, the process is analog to the one considered for the antennas MBF: we represent the pattern using spherical wave expansion and then interpolate it.

5.2 Results and discussion

In this section, we first present an analysis of the impact of noise on calibration accuracy. We study the noise on the position in a fashion similar to what has been done in the far-field chapter, as well as the noise on the attitude. Then, the computational time issue is addressed by considering the parallelization prospectives.

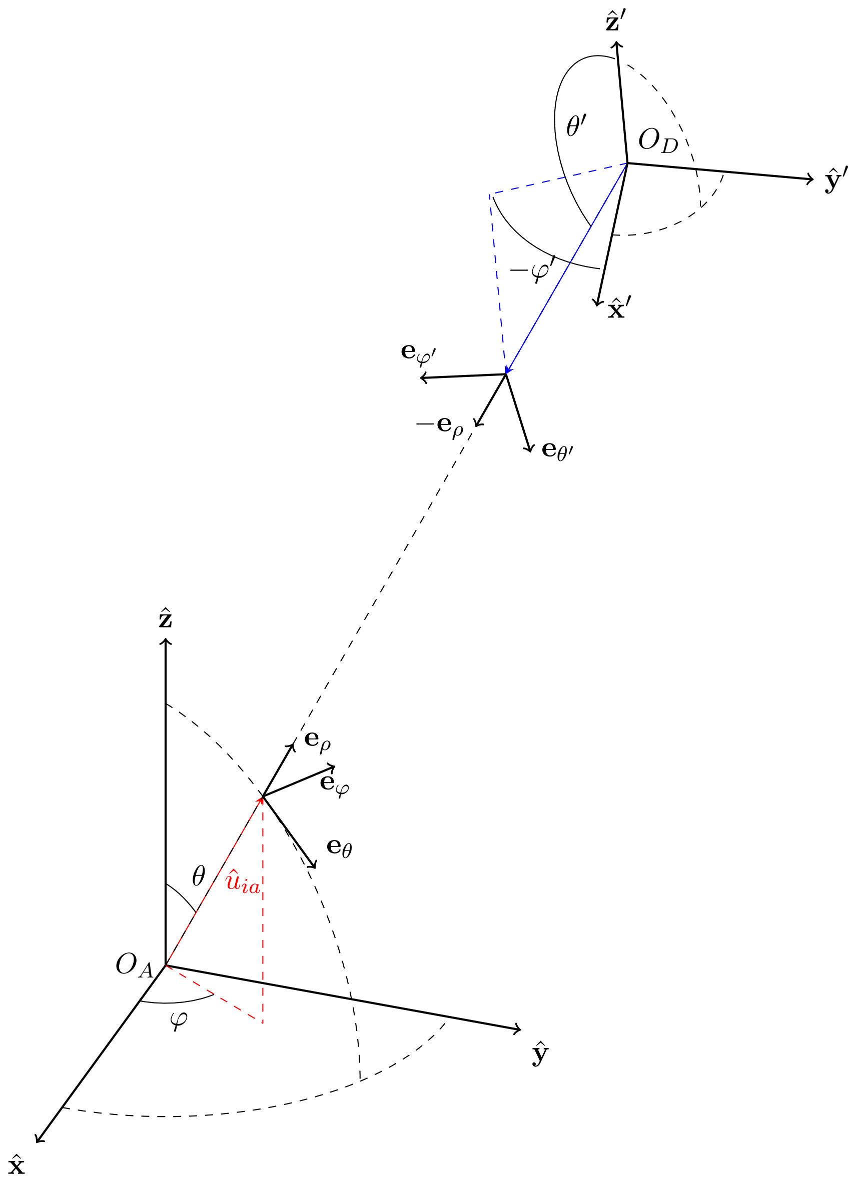

FIGURE 5.2: Direction of UAV dipole antennas.

5.2.1 Noise analysis

Two different noise sources are analyzed here: on the attitude and on the position. We consider Gaussian noise centered around the true value, i.e. unbiased. Recall that we are interested in *a posteriori* position. The noise then corresponds to the uncertainty on the measured position and attitude of the UAV.

Attitude noise analysis. We assess the impact of the noise acting on the UAV Tait-Bryan's angles. Table 5.1 gathers the simulations with random unbiased Gaussian noise with standard deviations σ_y, σ_p and σ_r for yaw, pitch and roll angles, respectively. We observe that the error due to an imprecise knowledge of the UAV attitude is weaker than absolute position error. Moreover, the error is mostly carried by the yaw angle. It comes from the fact that rotating

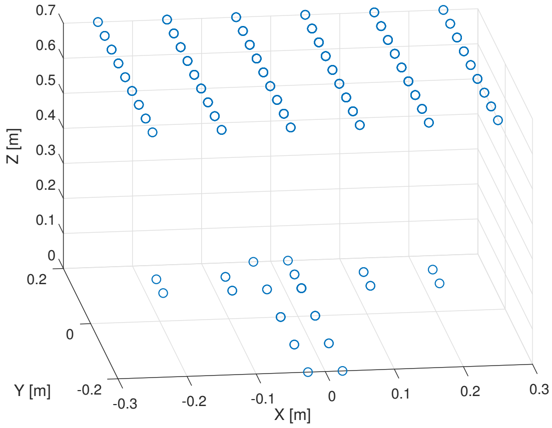

FIGURE 5.3: Mesh of the UAV simulated by Jean Cavillot. There are two feeds per antenna located in the center. The mesh consists of a horizontal plate (UAV core) mounted with two orthogonal dipole antennas.

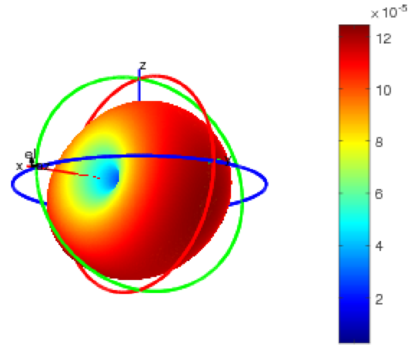

FIGURE 5.4: UAV pattern of the antenna along X. The used mesh is shown in Figure 5.3.

Max error (dB)	Mean error (dB)	σ_y	σ_p	σ_r	(degrees)
-48.14	-57.38	**2**	2	2	
-48.46	-59.62	**2**	0	0	
-54.32	-65.46	0	2	0	
-54.32	-65.14	0	0	2	

TABLE 5.1: Uncertainties about UAV attitude. Simulations obtained with spiral flight strategy at 10 m and $N_e = 512$. σ is given in degree.

around the X-axis (pitch) only perturbs the signal received on the Y-axis, and vice-versa for the Y-axis (roll).

Figure 5.6 illustrates the error rising when the knowledge on the attitude decreases. If the position is assumed to be exact, two regimes appear: a small noise level ($\sigma_a < 10$) is characterized by a linear relationship in logarithmic scale between the output error and the input noise. For $\sigma_a > 10$, very small nonlinear effects are observed. On the other hand, if the position is assumed to be inexact with fixed noise level $\sigma_e = 1\,\mathrm{cm}$, then we add a new regime: when the attitude noise ($\sigma_a \ll 1$) is dominated by the noise on position.

Position noise analysis. Careful investigation of Figure 5.5 lets us draw the same conclusions as in the previous case. The same two regimes appear with no-attitude noise. This time larger nonlinear effects are observed: for $\sigma_m > 0.5\,\mathrm{m}$ there is too much noise in the system and the true information is drowned. Besides, adding a fixed noise level on the attitude also adds a third regime.

Full noise analysis. Finally, we observe that the noise affecting mostly the system is the noise on position. Indeed, even if the attitude noise has the worst behaviour – it rises with $\sim 30 \left[\frac{\mathrm{dB}}{\mathrm{dec}}\right]$

compared with $\sim 20 \left[\frac{\text{dB}}{\text{dec}}\right]$ in the other case – the fact that it begins far below implies that it barely catches up the position noise. Moreover, we can conclude that no undesired coupling effect emerges when both noises are considered together. They sum up and henceforth, only the largest is significant. This being said, care should be taken about this behaviour because several non-considered aspects (SNR, environmental effects) may also increase this noise differently for attitude or position noises.

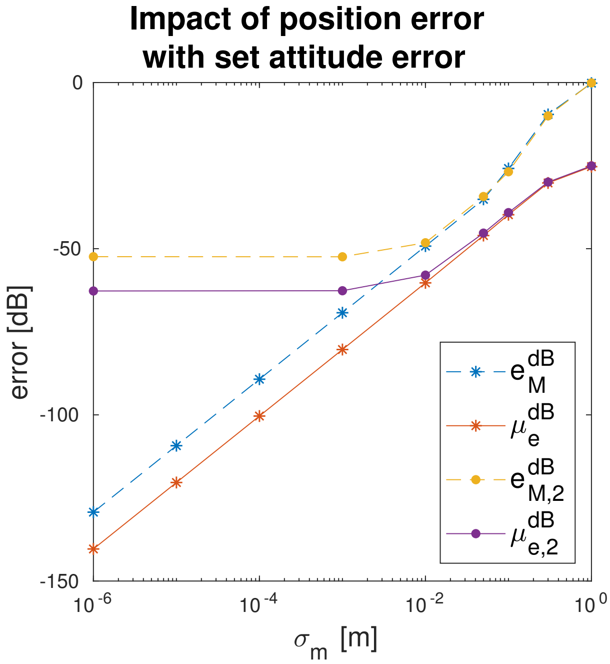

FIGURE 5.5: Error versus noise level on position with fixed attitude noise level. Spiral flight with $N_e = 512$. e_M^{dB} and μ_e^{dB} stand for max and mean error with accurate knowledge of attitude ($\sigma_a = 0$); Index "2" stands for inaccurate attitude knowledge: $\sigma_{a,2} = \begin{pmatrix}1 & 1 & 1\end{pmatrix}^T$.

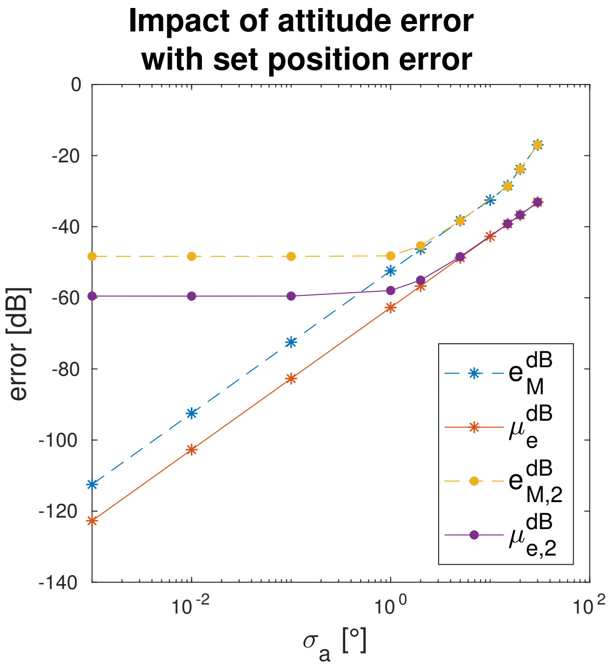

FIGURE 5.6: Error versus noise level on attitude with fixed position noise level. Spiral flight with $N_e = 512$. Attitude noise is increased similarly for three Tait Bryan's angles. e_M^{dB} and μ_e^{dB} stand for max and mean error with accurate knowledge on the position ($\sigma_e = 0$); Index "2" stands for inaccurate attitude knowledge: $\sigma_{e,2} = 1\,\text{cm}$.

5.2.2 Computational time concern

Let us first recall that this work is based on HARP. This tool is faster than alternative commercial software and relies on pre-computation. These computations should be processed for each frequency, but this must be done once and for all. We therefore do not include this pre-computation time because it is negligible from a calibration point of view: if the array is calibrated once a month, this pre-computation investment is very quickly returned. In the calibration procedure, two time-consuming parts emerge: first, creating the matrices $\mathbf{B}$ with spherical waves interpolation and second, solving the N_a optimization problem. Both of these tasks have a great parallelization potential and, therefore, the utilization of a cluster with up to N_a processors is highly recommended.

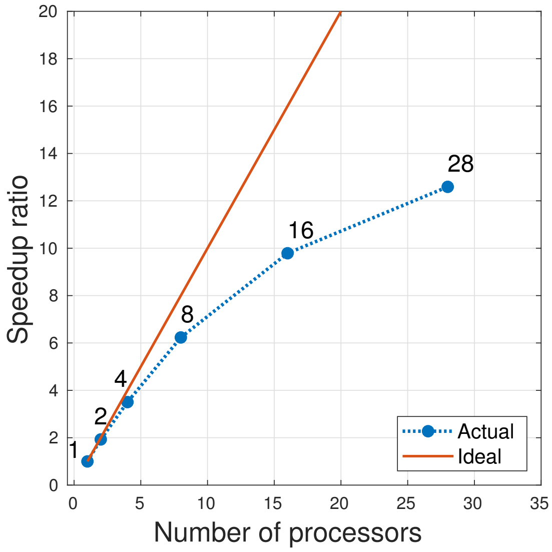

FIGURE 5.7: Speedup with parallel computing. Simulations with $N_e = 1024$ experiments.

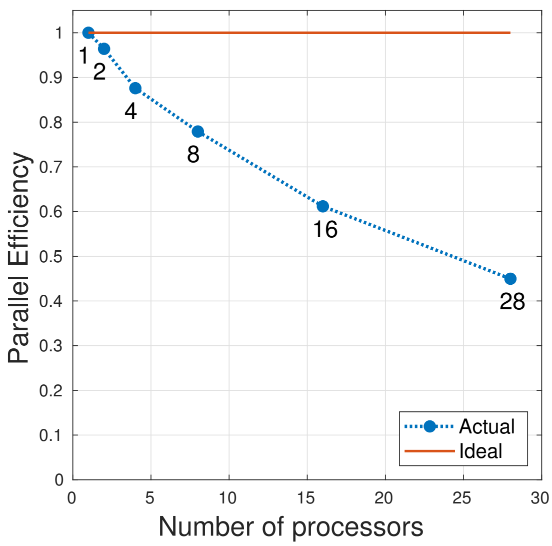

FIGURE 5.8: Efficiency of parallel computing. Simulations with $N_e = 1024$ experiments.

Figure 5.7 shows the time improvement of a parallelization. The initial computational time was 86 minutes and is now reduced to 6.8 minutes with 28 processors, hence leading to a speedup ratio of 12. Figure 5.8 displays the parallel efficiency defined as

$$\eta = \frac{T(1)}{n\,T(n)}\,, \tag{5.14}$$

where n refers to the number of processors and $T(n)$ refers to computational time needed when using n processors. Figure 5.8 shows that efficiency is smaller than 50%.

Here, we simply used the MATLAB parallelization framework but a more in-depth work could yield better outcomes. The used cluster has the following configuration:

System: Linux
CPU: 2x Intel Xeon E5-2660 v4 (14 cores @ 2.0 GHz – 28 threads – 35 MB cache)
Memory: 128 GB

5.3 Conclusion

The goal of the current chapter is to extend the UAV modelling: in the previous chapters the UAV attitude was assumed to be known. This too strong assumption is removed and the UAV attitude is taken into account. The proposed model is successively tested with noise on the position, noise on the attitude and finally noise on position and attitude. Based on the results, several conclusions are drawn:

- Two regimes are distinguished when only one noise source is active: linear (in dB) for small noise level, and small nonlinear effects for large noise level, i.e. the output noise depends mostly on the largest of both attitude/position noise.
- A third regime appears when combining both noise sources: for very small noise level, the error is constant.
- The noise on attitude is less significant than the noise on position although its slope is $10\,\mathrm{dB\,dec^{-1}}$ larger.
- This problem can easily be parallelized, hence leading to a significant reduction of the computation time.

Chapter 6

Regularization tools

Through this thesis, we encountered two situations with unsatisfying calibration outcomes related to an ill-conditioned system: in the far-field part when the UAV is not allowed to fly too far from the array center and in the near field with the cuts flight strategy. This chapter is devoted to improving these specific cases through *regularization*. Regularization is a procedure of introducing new information in order to solve an ill-posed problem or to avoid an overfitting phenomenon. Looking for instance at Figure 3.5, overfitting is observed: the data are perfectly "interpolated" in the region where we have some data and the error blows up anywhere else. An inspection carried out on the calibration coefficients shows that the coefficients are very high ($\approx 10^6$ in absolute value) compared with the expected solution (unitary coefficients). Due to the ill-conditioning of the system of linear equations, the coefficients are chosen such that the errors exactly cancel out in the narrow considered area. Hence, we can regularize by avoiding the coefficients to become too high, since this gives unphysical calibration outputs.

Three regularization methods are first introduced: the Tikhonov regularization, the truncated singular value decomposition (TSVD) and the least-squares minimization with a quadratic inequality constraint (LSQI). Then, several methods for choosing the regularization parameter are presented. Finally, the calibration outcomes with and without regularization are compared. The routines used to regularize come from the open-source package available in [28].

6.1 Regularization types

In this section and throughout the whole chapter, we deal with the following problem

$$\min_{\mathbf{x}\in\mathbb{R}^n} ||A\mathbf{x} - (\mathbf{b} + \epsilon\mathbf{f})||_2^2 \,. \tag{6.1}$$

This problem is similar to the ones obtained in previous chapters (see equation (3.5)): A has more lines (m) than columns (n) and the solution is not unique. Quantity $\epsilon\,\mathbf{f}$ is the perturbation vector and models the uncertainty on UAV position and attitude. In order to illustrate the main difficulties, we take a small numerical example from [28]. Let

$$A = \begin{pmatrix} 0.16 & 0.10 \\ 0.17 & 0.11 \\ 2.02 & 1.29 \end{pmatrix}, \quad (\mathbf{b} + \epsilon\mathbf{f}) = A \begin{pmatrix} 1 \\ 1 \end{pmatrix} + \epsilon \begin{pmatrix} 1 \\ -3 \\ 2 \end{pmatrix} = \begin{pmatrix} 0.27 \\ 0.25 \\ 3.33 \end{pmatrix} \tag{6.2}$$

with $\mathbf{b}$ being the exact right-hand side associated with the true solution $\mathbf{x}^\star = \begin{pmatrix} 1 & 1 \end{pmatrix}^T$ and $\mathbf{f}$ being a small perturbation with $\epsilon = 0.01$. Solving this problem in a classical way, e.g. Moore-Penrose inverse, yields the solution $\mathbf{x}_\epsilon = \begin{pmatrix} 7.0 & -8.3 \end{pmatrix}^T$ which is obviously too far from the true solution. This comes from the ill-conditioning of matrix A with condition number $\kappa(A) \approx 1000$. However, it can be shown [29] that

$$\frac{||\mathbf{x}^\star - \mathbf{x}_\epsilon||_2}{||\mathbf{x}^\star||_2} \leq \kappa(A)\,|\epsilon|\,\frac{||\mathbf{f}||}{||\mathbf{b}||} \tag{6.3}$$

with $\mathbf{f}$ being the perturbation vector, i.e. $\mathbf{f} = \begin{pmatrix} 1 & -3 & 2 \end{pmatrix}^T$. In this sense, the condition number measures the sensitivity of the problem $A\mathbf{x} = \mathbf{b}$.

6.1.1 Tikhonov regularization

The Tikhonov regularization is probably the most straightforward and used regularization with positive parameter λ. It can be stated as follows,

$$\min_{\mathbf{x}} ||A\mathbf{x} - \mathbf{b}||_2^2 + \lambda^2 ||\mathbf{x}||_2^2\,, \tag{6.4}$$

i.e. minimization of the residue with $\mathbf{x}$-2-norm penalty. This optimization problem is still convex and differentiable with respect to $\mathbf{x}$, the solution is therefore unique and characterized by the linear system of equations

$$A^{\mathrm{H}}(A\mathbf{x} - \mathbf{b}) + \lambda^2 \mathbf{x} = 0\,, \tag{6.5}$$

or equivalently by the least-squares problem

$$\begin{pmatrix} A \\ \lambda\, I_n \end{pmatrix} \mathbf{x} = \begin{pmatrix} b \\ 0 \end{pmatrix}. \tag{6.6}$$

Regularization parameter. Parameter λ acts directly on the $\mathbf{x}$-norm and prevents it from becoming too large. This is achieved by moving away from the least-squares solution. This can be viewed as avoiding overfitting because we prevent the outcome to stick unduly to the data. If $\lambda = 0$, the original un-regularized problem is retrieved. On the other hand, if $\lambda \to \infty$, the optimal solution is $\mathbf{0}$: the data has no importance. There is obviously a trade-off between both cases which is studied in Section 6.2: a good regularization parameter must balance the perturbation error (maximal when $\lambda = 0$) and the regularization error (maximal when $\lambda \to \infty$).

General case. Equation (6.4) can be generalized as

$$\min_{\mathbf{x}} ||A\mathbf{x} - \mathbf{b}||_2^2 + \lambda^2 ||L(\mathbf{x} - \mathbf{x}_0)||_2^2 \,. \tag{6.7}$$

Here L is often the identity matrix or a $p \times n$ discrete approximation of the $(n-p)$-th derivative operator [28]. In this chapter, the results are expressed according to the norm $||\mathbf{x}||_2$ (notably the L-curve, Section 6.2.1). A direct generalization is possible using the (semi)norm[1] $||L\mathbf{x}||_2$.

The $\mathbf{x}_0$ in Equation (6.7) stands for an initial estimate. In our case, a clever choice is a vector full of 1, i.e. the uncalibrated solution given by HARP. Notwithstanding, this case has not been considered in this work, because it naturally drives to the expected solution.

6.1.2 Truncated singular value decomposition (TSVD)

This regularization is based on the SVD of $A \in \mathbb{R}^{m \times n}$ given by

$$A = U \Sigma V^T = \sum_{i=1}^{n} u_i \, \sigma_i \, v_i^T \,, \tag{6.8}$$

with unitary matrices $U \in \mathbb{R}^{m \times m}$, $V \in \mathbb{R}^{n \times n}$ and diagonal matrix $\Sigma = \mathrm{diag}(\sigma_1, \ldots, \sigma_n)$ with singular values $\sigma_1 \geq \ldots \geq \sigma_n \geq 0$. The rank r of A is the number of positive singular values [30].

Using the SVD basis, the classical least-squares solution x_{LQ} can be written as

$$x_{LQ} = \sum_{i=1}^{r} \frac{u_i^T b}{\sigma_i} v_i \,. \tag{6.9}$$

As described in [29]: *"Due to the division by small singular values σ_i, the solution x_{LS} may be dominated by components associated with the errors in b."*. In order to stabilize the solution, the sum is truncated to $k < r$, hence leading to the TSVD solution

$$x_{TSVD} = \sum_{i=1}^{k} \frac{u_i^T b}{\sigma_i} v_i \,. \tag{6.10}$$

Link with Tikhonov. Writing the Tikhonov solution using the orthonormal basis given by the SVD it comes

$$x_T = \sum_{i=1}^{r} \frac{\sigma_i^2}{\sigma_i^2 + \lambda^2} \frac{u_i^T b}{\sigma_i} v_i \,. \tag{6.11}$$

This can be seen as a first-order *high-pass filter* suppressing too small singular values. On the other hand, the TSVD can also be seen as a sharp *high-pass filter*: either we select singular value i or not. The links between both regularizations are more detailed in [29].

[1] If L is a discrete approximation of the derivative operator, then the norm axiom $||\mathbf{x}|| = \mathbf{0} \Leftrightarrow \mathbf{x} = \mathbf{0}$ is not valid anymore (take $\mathbf{x}$ as a positive constant).

6.1.3 Least squares with a quadratic inequality constraint (LSQI)

The last studied regularization is the LSQI. It can be stated as

$$\min_{\mathbf{x}} ||A\mathbf{x} - \mathbf{b}||_2 \quad \text{subject to} \quad ||\mathbf{x}||_2 \leq \alpha \,, \tag{6.12}$$

α being the regularization parameter. This parameter is related to λ from Tikhonov regularization in a non-linear way. The solution of this problem can be computed as follows [28]: if $||\mathbf{x}_{LS}||_2 \leq \alpha$ then $\mathbf{x}_{LSQI} \leftarrow \mathbf{x}_{LS}$ and $\lambda \leftarrow 0$ else use an iterative scheme to solve

$$\min_{\mathbf{x}_\lambda} ||A\mathbf{x}_\lambda - \mathbf{b}||_2 \quad \text{subject to} \quad ||\mathbf{x}_\lambda||_2 = \alpha \tag{6.13}$$

for λ and $\mathbf{x}_\lambda$.

6.2 Choosing the regularization parameter

A significant aspect to take into account while talking about regularization is the parameter choice. Two main approaches can be examined: firstly, adjusting by hand the parameter until acceptable results are found. Secondly, computing *a priori* the best parameter with respect to a specific criterion. The first approach will give the best outcomes given that the parameter can be "perfectly" tuned. There are several drawbacks: a risk of overfitting the regularization parameter with respect to the training set and the need to tune this parameter for each different case. This is the reason why the second approach has been adopted in this work. It allows an automated selection of the parameter which is hence different for each UAV path, frequency, or even AUT.

This section first presents a graphical tool to analyze the regularization parameter: the L-curve [31]. Then the three selected criteria are explained and applied to a specific example of an ill-conditioned problem. A FF calibration with 256 experiments from a spiral flight strategy is assumed. The mathematical derivations and implementations can be found in [28, 31, 32].

6.2.1 The L-curve: a graphical tool to choose the regularization parameter

A very convenient tool used for the analysis of ill-posed problems is the so-called L-curve. This log-log plot shows the norm of the regularized solution ($||A\mathbf{x}_{reg} - \mathbf{b}||_2$) versus the norm of the corresponding residual norm ($||\mathbf{x}_{reg}||_2$). Doing so, the L-curve displays the trade-off between the regularization and perturbation error. It is called "L-curve" due to its shape which is commonly a "L". Figure 6.1 and 6.2 shows respectively the generic form of the L-curve and the specific form when applied on a FF spiral flight strategy.

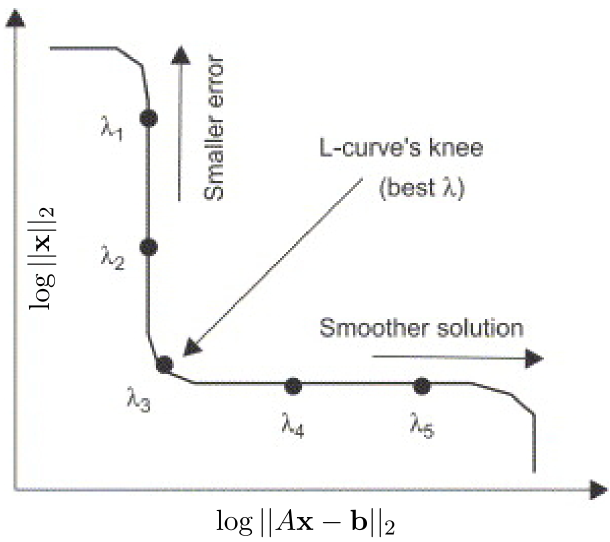

FIGURE 6.1: The generic form of the L-curve [33] with $\lambda_1 < \lambda_2 < \ldots < \lambda_5$.

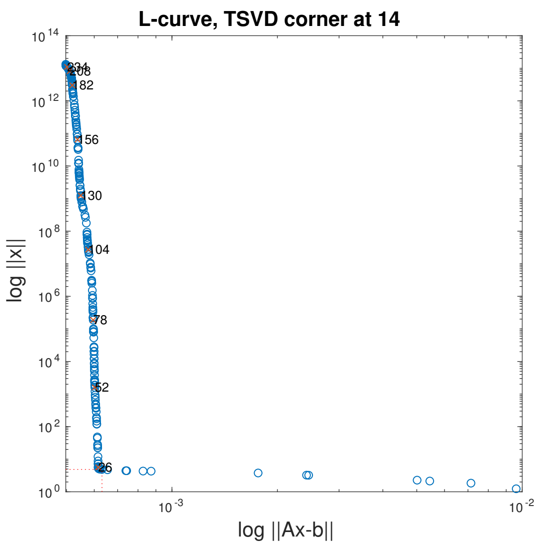

FIGURE 6.2: L-curve for a TSVD regularization of a FF spiral flight strategy. The numbers on the plot, associated with the red dots, stand for the k parameter value of the TSVD.

6.2.2 Parameter choice strategies

Discrepancy principle. This method is the only one based on an *a priori* knowledge on the norm of the perturbation error $||\mathbf{e}||_2$. It chooses the regularization parameter such that the regularized solution satisfies

$$||A\mathbf{x}_{reg} - \mathbf{b}|| = ||\mathbf{e}||_2 \,. \tag{6.14}$$

When a good guess for $||\mathbf{e}||_2$ is available, this method gives a good regularization parameter corresponding to a regularized solution immediately to the right of the L-curve corner [28], e.g. between λ_3 and λ_4 in Figure 6.1. The discrepancy principle can be only used for the LSQI.

In the present context, a good guess for the norm error is the solution obtained by HARP. It leads to a perturbation error

$$||\mathbf{e}||_2 = ||A\mathbf{x}_{HARP} - \mathbf{b}||_2 \,. \tag{6.15}$$

Generalized cross-validation (GCV). This method defined for continuous and discrete parameters is based on the idea that a left out element b_i should be well predicted by the regularized solution. This method works well for white noise, i.e. if all elements of the noise vector are unbiased and have the same variance [34]. This leads to the minimization of the GCV function

$$G = \frac{||A\,\mathbf{x}_{reg} - \mathbf{b}||_2^2}{(tr(\mathbf{I}_m - A\,A^I))^2} \,, \tag{6.16}$$

where tr stands for the trace function and A^I is a matrix producing the regularized solution when right-multiplied by $\mathbf{b}$, i.e. $\mathbf{x}_{reg} = A^I\mathbf{b}$ [28]. It can be shown that the GCV method amounts to tracking the characteristic L-curve corner [35].

Figure 6.3 illustrates the GCV function applied on the TSVD regularization in the case of a FF spiral flight strategy. A very large range of parameter values k give similar GCV values. This implies less robustness for this criterion when applied to the calibration problem.

Remark that this method is $||\mathbf{e}||_2$-free and requires no additional information. It allows the selection of the parameter for Tikhonov and TSVD regularization.

Quasi-optimality criterion. This method is, *stricto sensu*, only defined for a continuous regularization parameter λ. The parameter is chosen by minimizing

$$Q = \lambda \left|\left| \frac{d\mathbf{x}_\lambda}{d\lambda} \right|\right|_2 . \tag{6.17}$$

A more explicit formulation as well as a generalization for a non-continuous parameter λ is presented in [28]. A proof regarding the link between the quasi-optimality (QO) criterion and the goal of finding good balance between perturbation and regularization error is provided in [35].

Figure 6.4 illustrate the QO criterion applied on the TSVD regularization in the case of a FF spiral strategy. We see that the obtained minimum, $k = 12$ also belongs to the range where the values of GCV function are very small (Figure 6.3). Therefore, choosing the QO criterion satisfies two criteria: the QO and the GCV.

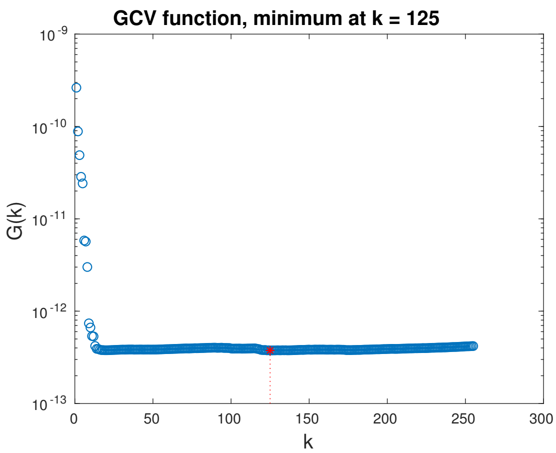

FIGURE 6.3: GCV function for a FF spiral flight strategy, the minimum is depicted in red and k refers to TSVD rank.

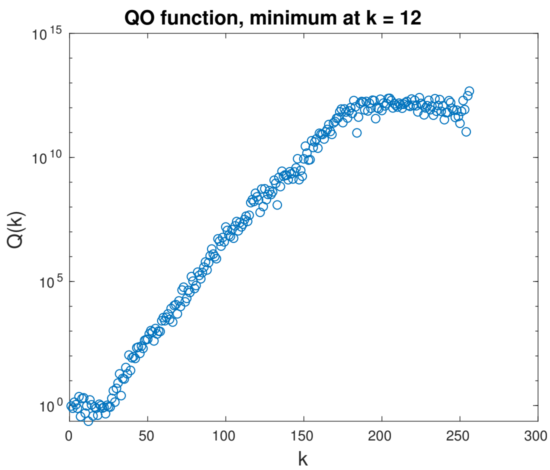

FIGURE 6.4: QO function for a FF spiral flight strategy, k refers to TSVD rank.

6.3 Results and discussion

This analysis has been made on the FF flight strategies and on the NF cut strategy: these are the cases where ill-conditioned systems appear. Using regularization on well-conditioned systems is not a good idea and will weaken the outcomes. Regularization results are gathered in Figure 6.5, a zoom on the best calibration errors is realized as the difference between a bad calibration (error $\approx 60\,\mathrm{dB}$) and a very bad (error $\gg 60\,\mathrm{dB}$) is not interesting. The first striking observation is that regularization clearly improves all the outputs. Preventing the calibration coefficients from being too large helps guiding the solution towards more accurate results. The best FF output consists in a LSQI regularization where the discrepancy principle is applied using a spiral strategy. However, the LSQI gives poor outcomes with other strategies. On the other hand, the QO strategy is the most stable one and yields, for each flight strategy, calibration performances that are nearly as good as the best one. We also observe that the QO works better on the TSVD. Finally, the GCV criterion applied to the TSVD gives the best output for grid, random, equi-spaced and cuts (in near field) but poorer performances elsewhere.

Notice that it is possible to estimate *a priori* whether a regularization will enhance the outcomes. Table 6.1 shows an example of the condition number of the matrix associated with the normal equations (3.9), denoted by $\mathbf{B}$ in the previous chapters. In the FF case and under the assumption of a restricted path, this condition number is significantly larger than the few hundreds obtained with NF strategies. Regularization is then highly recommended. The 8-cuts condition number is also larger than the others NF strategies (a factor six in this example), this suggests that regularization may improve the result.

	Flight strategy	κ
FF	Spiral	$1.2\ 10^9$
	Grid	$7\ 10^9$
	8-Cuts	$2\ 10^{12}$
	Random	$2\ 10^{10}$
	Equi-spaced	$1\ 10^9$
NF	Spiral	$1\ 10^3$
	Grid	950
	8-cuts	$6\ 10^3$
	Random	$1.2\ 10^3$
	Equi-spaced	650

TABLE 6.1: Example of condition numbers of the normal system of equations for various flight strategies. $N_e = 256$ and maximum distance is 200 m for FF strategies and 25 m for the NF strategies.

The use of regularization for the far field is undoubtedly useful. The near-field calibration with cut strategy is also significantly improved (up to approximately 15 dB) and the initial gap between the cut strategy with the others is filled by regularization.

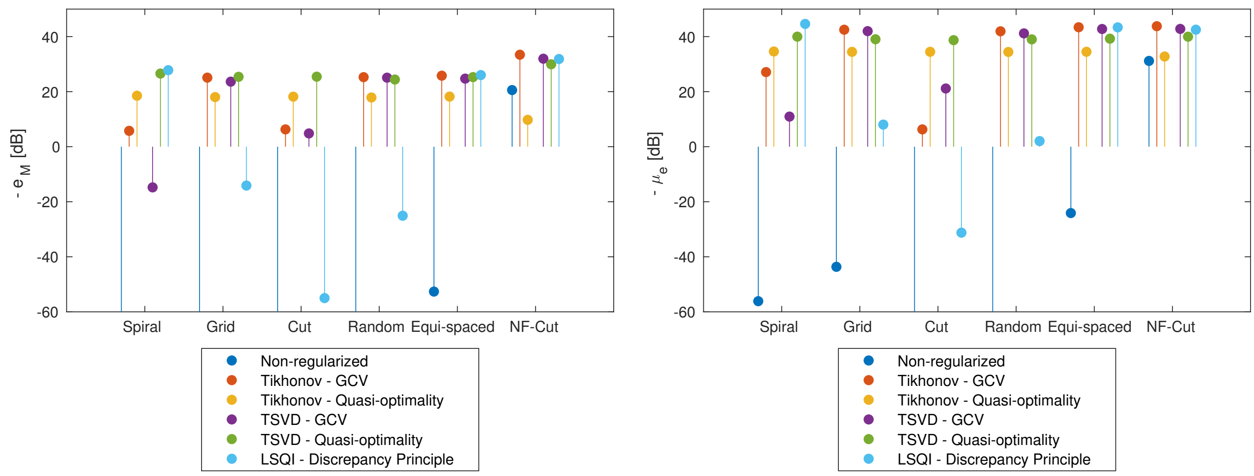

FIGURE 6.5: Several calibration outcomes with different regularizations and parameter choices. The opposite of the error are depicted such that the higher the point, the better. Left (resp. right) figure illustrates the max (resp. mean) error. The five first flight strategies are operated in FF (1000 m height) while the last one is in NF (10 m height).

6.4 Conclusion

Three regularization methods have been studied: Tikhonov, TSVD and LSQI. The link between these methods has been outlined. Then, three different criteria to find the regularization parameter have been presented: GCV, QO and discrepancy principle. The first two ones can be applied on Tikhonov and TSVD while the last one is applied on LSQI. A graphical tool allowing the study of these criteria, the L-curve, is introduced.

The outcomes of the regularization framework used on the ill-conditioned problems are satisfying: the FF calibration is improved by at least 80 dB and the NF calibration is improved by 15 dB. The fact that smaller improvements are observed for the NF calibration comes from the better conditioning of this problem compared with the FF case. The best result for the FF case is obtained with the LSQI method executed on a spiral flight strategy. However, the TSVD coupled with the quasi-optimality criterion is better in general as it gives a more stable calibration outcome, no matter the flight strategy.

Chapter 7

Conclusion

In the context of the Square Kilometre Array project, calibration is significantly important and experts have already expressed reservations with regard to the potential of self-calibration of such an array [6]. The SKA location in southern hemisphere also implies that fewer natural calibration sources are available. This leads naturally to the study of calibration with artificial sources. As this work demonstrates, the outcomes depend strongly on the noise level perceived on the Unmanned Aerial Vehicle position and attitude.

Far-field calibration. We have shown that calibration beyond the Fraunhofer distance has a main advantage: at that high altitude, the relative position error is negligible and the error is dominated by the attitude noise. This noise is less destructive: a realistic attitude noise level ([36]) gives maximum and mean error of $-50\,\mathrm{dB}$. The error levels obtained with unrestricted far-field flights are the best ones. Notwithstanding, several main issues arise: the SNR becomes worse with higher altitude and the sent pulses may badly interfere with other stations. This problem is significant for a core station (about 75% of SKA-low stations). Finally, the flight time is a scarce resource and may be wasted in a far-field calibration. Also, the need to cover wide angles leads to particularly large flight domains.

Near-field calibration. The same five flight strategies are studied in the context of a near-field calibration procedure. In Chapter 4, we have produced a model without taking into account the attitude. The aim of Chapter 5 is to extend this model. The analysis of both noise sources shows the dominant character of the position noise. Also, that an increase of the number of experiments yields satisfying pattern estimations: for instance a mean (resp. max) error of $-53\,\mathrm{dB}$ (resp. $-40\,\mathrm{dB}$) is obtained for 2048 experiments with an equi-spaced near-field strategy. Among the five flight strategies, four emerge as wise choices, i.e. spiral, grid, random and equi-spaced. The 8-cuts strategy is indeed too noise sensitive.

The spiral and equi-spaced strategies require a smaller flight-time. This motivates the use of one of these flight strategies in the context of a calibration campaign. Thanks to the extended model from Chapter 5, we do not need to make the hypothesis that the UAV is parallel to the polarization directions. Hence flying approximately in a circle, as required by the equi-spaced strategy, is not a problem.

We have also shown the emerging trade-off about the covering flight area size. A too small area implies that boundary antennas have no data point in some directions and a too large area induces a lot of redundant and not valuable points.

Regularization. In the case of a far-field campaign with restricted flight time, or if only cut strategies are practicable, regularization enables a huge enhancement of the calibration. The ill-conditioned problems can be processed with different tools. A truncated SVD regularization with quasi-optimality criterion yields satisfactory results with no dependency on the flight strategy. The improvement is extremely large, i.e. up to 80 dB. The maximum error reaches -20 dB (resp. -30 dB) for the far-field (resp. near-field) case and the mean error reaches -40 dB for both cases.

Perspectives. As calibration must be performed for each station and each frequency, it is clear that computational time is an important issue. Hence, acceleration of the computations may be further investigated in future works. For instance, a more in-depth parallelization analysis might yield an improvement.

Also, the obtained errors could be reduced by weighing the measurements according to their relevance. For instance, for near-field calibration, measurements in the center of the array are greatly beneficial for the entire array while measurements far from the center only help a small subset of antennas.

Finally, the model should be extended in order to take into account other acquisition noises, such as the thermal noise of the measure instruments and propagation errors (multipath interferences inducing fading, external interferences, etc.).

It is certain that calibration will have a major role to play in the future works about the SKA and this project is more up-to-date than ever: the first SKA-low prototype station has been completed on site two weeks before the release of this work [4]. Exciting efforts will be done about this first station and it is sure that calibration is going to be part of them.

Bibliography

[1] The SKA organisation, “Square kilometer array,” 2018. [Online]. Available: https://www.skatelescope.org/. [Accessed: May 16, 2018].

[2] E. de Lera Acedo *et al.*, “SKA aperture array verification system: electromagnetic modeling and beam pattern measurements using a micro UAV,” *Experimental Astronomy*, vol. 45, pp. 1–20, Mar. 2018.

[3] G. Pupillo *et al.*, “Medicina array demonstrator: calibration and radiation pattern characterization using a uav-mounted radio-frequency source,” *Experimental Astronomy*, vol. 39, pp. 405–421, June 2015.

[4] ASTRON, “First ska-low prototype station completed on site,” May 2018. [Online]. Available: http://www.astron.nl/first-ska-low-prototype-station-completed-site. [Accessed: May 30, 2018].

[5] Swinburne University of Technology, “Radio interferometer – the SAO encyclopedia of astronomy,” 2018. [Online]. Available: http://astronomy.swin.edu.au/cosmos/R/Radio+Interferometer/. [Accessed: June 4, 2018].

[6] C. Lonsdale, “Calibration approaches,” MIT Haystack, Tech. Rep. LFD memo 015, Dec. 2004.

[7] N. Hurley-Walker, “Post-graduate research projects,” 2017. [Online]. Available: https://astronomy.curtin.edu.au/wp-content/uploads/sites/5/2017/07/CIRA-2017_2018-PhD-Project-Outlines-Booklet.pdf. [Accessed: May 25, 2018].

[8] S. Wijnholds, S. Tol, R. Nijboer, and A.-J. Van Der Veen, “Calibration challenges for the next generation of radio telescopes,” *IEEE Signal Processing Magazine*, vol. 27, pp. 30–42, Mar. 2010.

[9] S. J. Wijnholds and A. J. van der Veen, “Multisource self-calibration for sensor arrays,” *IEEE Transactions on Signal Processing*, vol. 57, pp. 3512–3522, Sept 2009.

[10] J. Radcliff, “Self calibration - newton DARA,” 2016. [Online]. Available: http://www.jb.man.ac.uk/~radcliff/DARA/DARA_links/Zambia2016/L9.pdf. [Accessed: May 25, 2018].

[11] E. Acedo, C. Craeye, N. Razavi-Ghods, and D. Gonzalez-Ovejero, “Low order beam models for the calibration of large aperture arrays for radio astronomy; the case of the ska-low instrument,” pp. 1182–1185, Electromagnetics in Advanced Applications (ICEAA), 2013.

[12] G. Virone, F. Paonessa, O. Antonio Peverini, G. Addamo, P. Bolli, and E. Acedo, “Uav-based technique for the characterization of the intrinsic cross-polarization ratio (ixr),” pp. 3825–3828, European Conference on Antennas on Propagation (EUCAP), Mar. 2017.

[13] G. Virone, A. M. Lingua, M. Piras, A. Cina, F. Perini, J. Monari, F. Paonessa, O. A. Peverini, G. Addamo, and R. Tascone, “Antenna pattern verification system based on a micro unmanned aerial vehicle (uav),” *IEEE Antennas and Wireless Propagation Letters*, vol. 13, pp. 169–172, 2014.

[14] G. Hislop, C. Craeye, and D. Gonzalez-Ovejero, “Antenna calibration for near-field material characterization,” *IEEE Transactions on Antennas and Propagation*, vol. 64, pp. 1–1, April 2016.

[15] D. Gonzalez-Ovejero and C. Craeye, “Interpolatory macro basis functions analysis of non-periodic arrays,” *IEEE Transactions on Antennas and Propagation*, vol. 59, pp. 3117–3122, 08 2011.

[16] H. Bui-Van, J. Abraham, M. Arts, Q. Gueuning, C. Raucy, D. Gonzalez-Ovejero, E. de Lera Acedo, and C. Craeye, “Fast and Accurate Simulation Technique for Large Irregular Arrays,” *IEEE Transactions on Antennas and Propagation*, vol. 66, pp. 1805–1817, Apr. 2018.

[17] Microwave Studio, “Cst,” 2015. [Online]. Available: `https://www.cst.com/`.

[18] E. S. Software, “Wipl-d.” [Online]. Available: `https://www.wipl-d.com/`.

[19] W. C. Gibson, *The Method of Moments in Electromagnetics*, ch. 3. Chapman and Hall/CRC, 2014.

[20] M. S. Neiman, “The principle of reciprocity in antenna theory,” *Proceedings of the IRE*, vol. 31, pp. 666–671, Dec. 1943.

[21] A. Ludwig, “The definition of cross polarization,” *IEEE Transactions on Antennas and Propagation*, vol. 21, no. 1, pp. 116–119, 1973.

[22] P. M. L. Tammes, “On the origin of number and arrangement of the places of exit on the surface of pollen-grains,” *Recueil des travaux botaniques néerlandais*, vol. 27, no. 1, pp. 1–84, 1930.

[23] M. Born and E. Wolf, *Principles of Optics*, ch. 8. New York City: Pergamon Press, 1965.

[24] R. E. Blahut, *Theory of Remote Image Formation.* Cambridge University Press, 1 ed., Jan. 2005.

[25] US army, “Uas roadmap,” 2010. [Online]. Available: `http://www.rucker.army.mil/usaace/uas/US%20Army%20UAS%20RoadMap%202010%202035.pdf`. [Accessed: May 16, 2018].

[26] E. de Lera Acedo, N. Razavi-Ghods, N. Troop, N. Drought, and A. J. Faulkner, “Skala, a log-periodic array antenna for the ska-low instrument: design, simulations, tests and system considerations,” *Experimental Astronomy*, vol. 39, pp. 567–594, Oct. 2015.

[27] L. Landau and E. M. Lifshitz, *Mechanics (3rd ed.)*. Oxford: Butterworth-Heinemann, 1996.

[28] P. C. Hansen, “Regularization tools - a Matlab package for analysis and solution of discrete ill-posed problems,” Mar. 2008.

[29] G. Golub and C. Van Loan, *Matrix Computations*. Johns Hopkins Studies in the Mathematical Sciences, Johns Hopkins University Press, 1996.

[30] R. D. Fierro, G. H. Golub, P. C. Hansen, and D. P. O’Leary, “Regularization by truncated total least squares,” *SIAM Journal on Scientific Computing*, vol. 18, no. 4, pp. 1223–1241, 1997.

[31] P. C. Hansen, “The truncated svd as a method for regularization,” *BIT Numerical Mathematics*, vol. 27, pp. 534–553, Dec. 1987.

[32] P. C. Hansen, “The l-curve and its use in the numerical treatment of inverse problems,” July 1999.

[33] E. Santos and A. Bassrei, “L- and theta-curve approaches for the selection of regularization parameter in geophysical diffraction tomography,” *Computers and Geosciences*, vol. 33, no. 5, pp. 618 – 629, 2007.

[34] A. Schuhmacher, J. Hald, K. B. Rasmussen, and P. C. Hansen, “Sound source reconstruction using inverse boundary element calculations,” *The Journal of the Acoustical Society of America*, vol. 113, no. 1, pp. 114–127, 2003.

[35] P. C. Hansen, “Analysis of discrete ill-posed problems by means of the l-curve,” *SIAM Review*, vol. 34, no. 4, pp. 561–580, 1992.

[36] M. Gowda, J. Manweiler, A. Dhekne, R. R. Choudhury, and J. D. Weisz, “Tracking drone orientation with multiple gps receivers,” in *Proceedings of the 22Nd Annual International Conference on Mobile Computing and Networking*, MobiCom 2016, (New York, NY, USA), pp. 280–293, ACM, 2016.

Rue Archimède, 1 bte L6.11.01, 1348 Louvain-la-Neuve www.uclouvain.be/epl